Particle Layer Effects on Flowfield and Infrared Characteristics of Aircraft Exhaust Plume

Yu-Ryeol Lee*, Ji-Won Lee*, Chang-Min Shin*, Jae-Won Kim†, R. S. Myong‡

*,‡School of Mechanical and Aerospace Engineering, Gyeongsang National University, Jinju, Gyeognam 52828, Republic of Korea

†Aerospace Technology Research Institute, Agency for Defense Development, Daejeon 34188, Republic of Korea

‡Corresponding author: *myong@gnu.ac.kr* (R. S. Myong)

Abstract

Most existing plume IR suppression techniques are difficult to apply to an already established aircraft system and cannot be applied in an active way. As an alternative solution, the present study explores an active technique for shielding IR signals by injecting particles into the engine exhaust plume. A Eulerian-Lagrangian-based discrete phase method was used to calculate a multiphase flow composed of exhaust gas and injected particles. In order to analyze the characteristics of thermal flow and particle distribution under flight conditions, a cruise condition of Mach number 0.7 at an altitude of 20,000 ft was considered. Water droplets and carbon particles with diameters of 5 and 10 μm were considered, and placed randomly within the particle layer. To analyze the shielding effect according to particle size, material type, and distribution pattern, the transmittance of IR electromagnetic waves of 3~5 μm wavelength was analyzed using a Maxwell multi-level fast multipole method. When the total mass was kept the same, 5 μm water droplets in wavelength bands below 3.5~3.7 μm, and 10 μm water droplets or 5 μm carbon particles in wavelength bands above 3.5~3.7 μm were more effective for shielding. If the single layer transmittance information obtained in the present study is extended to actual particle layers of several tens of centimeters, it is expected that the shielding effect will be significantly higher.

---

*Graduate Student, School of Mechanical and Aerospace Engineering, 501 Jinjudaero, Gyeongnam.
†Research Engineer, P.O. Box 35, Yuseong.
‡Professor, School of Mechanical and Aerospace Engineering and Research Center for Aircraft Core Technology, 501 Jinjudaero, Gyeongnam; myong@gnu.ac.kr. Associate Fellow AIAA (Corresponding Author).

1. Introduction

In the modern battlefield, infrared (IR) tracking missiles detect and track high intensity infrared signals that are self-emitted and reflected from aircraft. This is in contrast to radar-tracking missile systems that first emit electromagnetic waves in the direction of the aircraft and then detect and track the signal when it is reflected from the aircraft surface. Because pilots are not aware when their aircraft has been locked-on by a passive infrared tracking missile, it poses a greater threat to aircraft survivability.

The IR signals of various wavelength bands can be generated by an aircraft during flight. The main sources of IR signals are shown in Fig. 1. IR signals are mainly produced by hot engine parts, exhaust gas, aerodynamic heating of the airframe and intake, sunlight and moonlight reflected by the aircraft surface, and anti/de-icing systems [1].

IR signals from engine exhaust gas are mainly generated by high-temperature carbon dioxide (CO_2) and water vapor (H_2O), which are products of engine combustion. The exhaust gas IR signal has a discrete set of characteristic signal wavelength. Specifically, the polyatomic gas molecules generate high intensity mid-wave infrared (MWIR) signals. The characteristics of the MWIR generated from aircraft exhaust gas are summarized in Fig. 2. MWIR signals from engine exhaust gas are mainly generated in wavelength bands between 3~5 μm, for example, at 4~4.4 μm by CO_2, and these are the main IR sources detected by IR tracking missiles [1]. To enhance aircraft survivability, therefore, it is necessary to reduce the MWIR signals generated by engine exhaust gas.

A number of studies have been conducted on methods to reduce IR signals generated from aircraft exhaust gas, for example, by reducing the temperature of the exhaust gas, or shielding the high temperature part using bypass air, a serpentine nozzle, or aft-deck. Various studies have also been actively conducted on how the serpentine nozzle design parameters affect thrust, thermal flow field and IR reduction [2-7]. It was shown by Sun *et al*. [2] and Shan *et al*. [7] that as the ratio of shielding of the hot part of the engine in the nozzle increased, the IR signal decreased, but at the same time the thrust penalty increased.

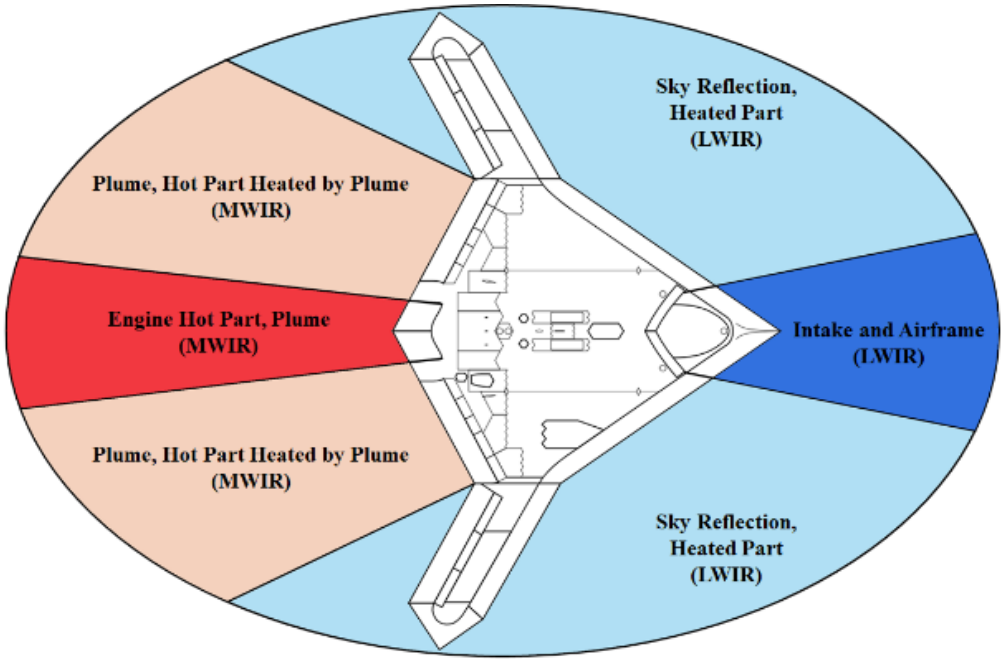

Fig. 1. Dominant IR sources of X-47B UCAV.

Recently, an experiment was conducted to measure the characteristics of the IR signal generated by exhaust gas using a turbojet engine with kerosene fuel [8,9]. Since it is expensive to measure the IR signal of exhaust gas for a large aircraft engine, a micro turbojet engine was used instead. The flow characteristics of the exhaust gas plume were also experimentally analyzed through schlieren visualization [10]. The IR signal was measured while the bypass ratio and observation angle were changed [11]. In addition, a study was conducted using a computational method for imaging aircraft IR [12].

In a serpentine nozzle, exhaust gas and bypass air mixing occurs more actively due to the curvature of the nozzle centerline. When the mixing of hot exhaust gas and cold bypass air was increased, the average temperature at the nozzle exit became lower than that of a conventional axisymmetric nozzle [13,14]. A study was conducted to calculate the IR signal from exhaust gas, non-gray gas, and solid surface sources using computational analysis [15]. In addition, a study was conducted on how changing the concentration of molecules constituting the exhaust gas affected the IR signal characteristics [16].

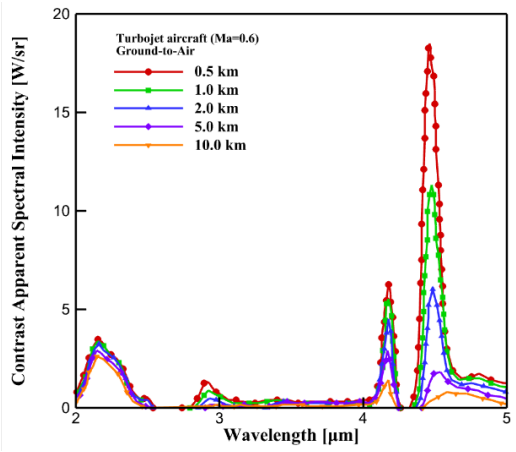

(a) Characteristics of plume IR signal

	Mistral	Strela-2M	Igla	Stinger
Country	Europe	Russia	Russia	USA
Detection Wavelength	2-4/ 3.5-5 μm	1.7-2.8 μm	3-5 μm	3-5 μm
Flight Mach	Max. 2.5	Max. 1.3	Over 2	Max. 2.2

(b) Specification of MANPADS

Fig. 2. Characteristics of MWIR.

Despite extensive efforts to reduce IR signals, the IR reduction techniques developed so far suffer from penalties including high cost and thrust loss. In the case of a serpentine nozzle, the basic idea is to make it difficult for the IR seeker to detect engine hot spots by increasing the curvature of the nozzle centerline. However, manufacturing a serpentine nozzle is difficult due to its curvature and complex geometry. Furthermore, it is difficult to shield the hot part of the engine from all angles, and the curvature of the nozzle centerline cannot be increased indefinitely without incurring a penalty for thrust.

Above all, the biggest limitation of existing techniques is that they are difficult to fit to an already established aircraft system, and cannot be applied in an active way. As an alternative solution, the present study explored an active technique for shielding IR signals by injecting particles into the engine exhaust plume.

As summarized in Table 1, several previous studies [17-28] have investigated methods to reduce the IR signal generated from exhaust gas using particle injection. These studies investigated the basic principle of the IR reduction technique using experimental and theoretical methods.

Marteney [17] investigated IR reduction through particle injection in the Rayleigh region, where the particle size is very small compared to the wavelength of the IR signal. Krascella [18] calculated the transmittance of a single particle using the Mie theory, derived for the case where

the particle size is similar to the wavelength of the IR signal. Harris *et al*. [19] performed theoretical and experimental studies to measure the synergistic absorption of hot gas radiation by an aerosol/absorbing gas mixture, and to verify the IR absorption of carbon particles. Weisrose and Shadmon [20] presented a method of calculating radiative transfer through an aerosol cloud, including multiple and inelastic scattering effects. Weirose *et al*. [21] conducted an experiment in which an aerosol cloud was injected into the air stream surrounding the exhaust jet flow. They found that the IR radiation emitted by the exhaust system and gaseous plume was substantially reduced at all aspect angles. They also estimated the attenuation of the IR radiation by the aerosol cloud using an aerosol cloud reduction factor which describes the passage of IR radiation through an aerosol cloud.

Table 1. Review of previous works on IR suppression based on particle injection.

Authors (Year)	Method & Model	Scattering Region	IR Source	Flight Condition	Particle Material
Marteney (1965) [17]	Experiment	Rayleigh	Radiation Beam	Ground	Carbon / Tungsten
Krascella (1965) [18]	Mie Theory	Rayleigh, Mie	Radiation Beam	Ground	Carbon / Silicon / Tungsten
Harris *et al.* (1979) [19]	Aerosol Cloud Approximation, Experiment	Rayleigh, Mie	Kerosene Burner	Ground	N_2O (Gas), Carbon, TiO_2
Weirose *et al.* (1984) [20]	Aerosol Cloud Approximation	Rayleigh, Mie	Radiation Beam	Ground	Carbon
Weirose *et al.* (1988) [21]	Experiment	Mie	Turbofan	Ground	Carbon
Parent *et al.* (2006) [22]	Experiment	Optical	Radiation Beam	Ground	Water
Chen *et al.* (2011) [23]	Monte Carlo Method	Mie	Radiation Beam	Ground	Water
Voitsekhovskaya *et al.* (2014) [24]	Aerosol Approximation	Rayleigh, Mie	Radiation Beam	Ground	Water

Myer *et al.* (2014) [25]	Experiment	Rayleigh, Mie	Radiation Beam	Ground	Sodium Nitrate
Li *et al.* (2015) [26]	Experiment	Optical	Turbojet (Kerosene)	Ground	Water
Liu *et al.* (2019) [27]	Aerosol Cloud Approximation	Mie	Turbofan	Ground	Water
Lee *et al.* (2020) [28]	DPM (Flow)	Optical	Turbojet	Ground	Water
Present	DPM (Flow), Full Maxwell	Mie	Turbofan	Ground, Cruise Flight	Water, Carbon

Parent *et al*. [22] experimentally investigated IR radiation attenuation using a water spray and measured the spectral transmissivity of water particles. Chen *et al*. [23] calculated the IR transmission of water particles using the Monte Carlo method and analyzed the effect of varying droplet diameters. Voitsekhovskaya *et al*. [24] performed a numerical study of the gas-aerosol transmission in the IR range for various optical and microphysical parameters. Myer *et al*. [25] measured the reflectance spectra of sodium nitrate in the 1.3–16 micron range and found that particle size had a significant influence on the measured reflectance spectra. Li *et al*. [26] investigated the concept of injecting water into a rocket exhaust plume to reduce the jet temperature and conducted a series of experiments in a controlled laboratory environment. Liu *et al*. [27] calculated the attenuation of IR radiation energy by ship water mist. Lee *et al*. [28] calculated the exhaust gas and particle flow of aircraft turbojet engines by injecting particles in stationary ground conditions.

Except for Weirose *et al*. [21] most of the studies conducted experiments using a radiation beam or burner that generated an IR signal in a specific wavelength band, since it is difficult to use an actual aircraft engine. Experiments using a radiation beam in a stationary situation like this are limited when it comes to describing the interaction between the exhaust plume of an aircraft and the injected particles during flight. Moreover, previous theoretical studies [19,20,24,27] calculated the transmittance of IR signals with particles using an approximate technique such as aerosol cloud approximation.

The approximate technique calculates transmittance by assuming that the injected particles are one cloud. The number of times the incident IR signal meets the particles is predicted, considering the amount of particles injected. Using the predicted number of times, the reduction of the IR signal by the particle is then calculated, and the transmittance of the entire aerosol cloud is finally calculated.

But the approximate technique only calculated the transmittance of the cloud using injected particles in a stationary state. This means the existing approximate method has difficulty considering how the high-speed exhaust gas of an aircraft in flight affects the distribution and concentration of particles. Also, in the resonant region where the size of the particle is similar to the wavelength of the IR signal generated from the exhaust gas, the accuracy of the approximate technique for particle scattering tends to decrease.

The goal of this work is two-fold: 1) to develop a multiphase flow method to describe the interaction between the exhaust plume and the injected particles in flight, as well as a full Maxwell electromagnetic method to accurately describe the attenuation of MWIR signal by particles in the resonance region, and 2) to investigate the effects of the particle layer on the IR and thermal flow characteristics of an aircraft exhaust plume.

First, we developed a multiphase flow method based on the discrete phase model (DPM) and investigated the effects of particle diameter and concentration on the flow characteristics of an exhaust gas plume. In order to analyze the characteristics of flow and particle distribution under flight conditions, a cruise flight condition of Mach number 0.7 at an altitude of 20,000 ft was considered. The scattering problem in the resonance region where the particle diameter and the IR signal wavelength are of the same order was then solved using one of the most efficient methods of moment (MoM) solvers, the multi-level fast multipole method (MLFMM). For particles randomly distributed for a given mass, the near-field scattering was computed using the MLFMM and then the transmittance of particle layer in the MWIR region was calculated. Further, by changing the size, number, and type of the particles, the transmittance characteristics of the particle layer were analyzed.

2. Methods to investigate IR attenuation through a particle layer

2.1. Previous approximate methods: Cloud approximations

Harris *et al*. [19] theoretically studied the reduction in the IR signal of a gas plume by the scattering and absorption of a particle layer. They divided the particle cloud into multiple layers using an optical depth to calculate the reduced IR signal as it passed through the particle layer. The final transmittance was obtained by calculating the decrease as it passed through the layer, based on the following formula,

$$\frac{dI(\tau,\mu,\phi)}{d\tau} = I(\tau,\mu,\phi) - w(\tau)J(\tau,\mu,\phi), \tag{1}$$

$$\text{where } J(\tau,\mu,\phi) = B(\tau,\mu,\phi) + \frac{1}{4\pi}\int_{-1}^{1}\int_{0}^{2\pi} P(\tau,\mu,\phi,\mu',\phi')I(\tau,\mu',\phi')d_{\mu'}d_{\phi'}, \tag{2}$$

$$B(\tau,\mu) = \frac{1}{2}\int_{0}^{1} P(\tau,\mu,\mu_1)e^{-\tau/\mu_1}d\mu_1, \tag{3}$$

$$P(\tau,\mu,\phi,\mu',\phi') = \sum_{n=1}^{N} P^N(T,\mu,\mu')\cos(n-1)(\phi'-\phi). \tag{4}$$

Equation (1) represents the basic radiative transfer equation for monochromatic radiation where $I(\tau,\mu,\phi)$ is the intensity of radiation at position τ in the direction $\mu = \cos\theta$, ϕ where θ,ϕ are the angle normal to the slab and the azimuth angle of an arbitrary meridian plane, respectively. The albedo of single scattering $w(\tau)$ is defined as the fractional change in τ due to scattering. The $J(\tau,\mu,\phi)$ represents the source function and is given by Eq. (2). The radiation model (3) stands for an isotropic radiator. The $P(\tau,\mu,\phi,\mu',\phi')$ in Eqs. (2)-(4) represent the phase function of scattering by particles and can be expressed in the Fourier series form where T is the so-called turbidity factor of the fraction of total scattering due to Mie scattering.

To calculate the transmittance due to multiple scattering, it is assumed that diffuse radiation does not occur at both ends of the medium. Equations (1)-(4) were calculated according to the optical depth layer to obtain the transmitted IR intensity in the final layer. The IR signal passing through the medium with pure scattering particles decreased as the optical depth increased. As the concentration of particles increased, the probability of scattering and back-scattering increased,

resulting in a decrease in IR signal transmittance.

The reduction in IR signal by the scattering and absorption of particles was also studied theoretically by Weisrose and Shadmon [20]. They calculated the radiative transfer through an aerosol cloud while including multiple and inelastic scattering effects. In order to calculate the scattering of the radiation signal, they introduced the scattering integral *S* and associated equations, as follows,

$$S = \int_0^{\pi} f_k(\theta) I(z,\theta) \sin(\theta) d\theta , \tag{5}$$

$$I(z) = I_0(z) + \sum_{k\geq 1} I_k(z) = I_0^+(z) + I_0^-(z) + \sum_{k\geq 1} \left(I_k^+(z) + I_k^-(z) \right), \tag{6}$$

$$\begin{aligned} \frac{dI_k^+(z)}{dz} &= -N(\sigma_a + \sigma_s) I_k^+(z) + \frac{N\sigma_s}{2} \left[I_{k-1}^+(z) \int_0^{\pi/2} f_k(\theta) \sin(\theta) d\theta + I_{k-1}^-(z) \int_{\pi/2}^{\pi} f_k(\theta) \sin(\theta) d\theta \right], \\ \frac{dI_k^-(z)}{dz} &= N(\sigma_a + \sigma_s) I_k^-(z) - \frac{N\sigma_s}{2} \left[I_{k-1}^-(z) \int_0^{\pi/2} f_k(\theta) \sin(\theta) d\theta + I_{k-1}^+(z) \int_{\pi/2}^{\pi} f_k(\theta) \sin(\theta) d\theta \right], \end{aligned} \tag{7}$$

$$f_k(\theta) = \frac{1}{4\pi} \sum_m \frac{a_m^k}{(2m+1)^{k-1}} P_m(\cos\theta) . \tag{8}$$

Here $I(z,\theta)$ is the radiation flux reaching the scatter at angle θ, with respect to a line-of-sight (LOS), and at location z. $f_k(\theta)$ is the angular scattering distribution of the *k*-th scattering at angle θ. $I_0(z)$ denotes non-scattered radiation and $I_k(z)$ represents the radiation intensity when scattering occurs *k* times. In multiple scattering by multiple particles in the aerosol cloud, the total radiation $I(z)$ is defined as Eq. (6). σ_a, σ_s, P_m are the absorption cross section, the scattering cross section, and the Legendre functions, respectively. The transmittance of the aerosol cloud can be calculated by solving Eqs. (5)-(8).

2.2. Previous experimental methods

A number of experimental studies have been conducted to study how the IR signal is attenuated by particle injection. Harris *et al*. [19] measured the synergistic absorption of hot gas radiation using an aerosol/absorbing gas mixture. They also analyzed the transmittance of an IR signal using a radiation beam to N_2O (gas) and carbon particle (solid) layers. It was observed that the transmittance decreased as the particle mass increased, and it was lowest when the particle size was similar to the wavelength of the electromagnetic wave. When N_2O and carbon particles with

a size parameter ($2\pi r / \lambda$) of 0.1 were compared under the same mass concentration conditions, the carbon particles showed a lower transmittance than N_2O. This is because solid particle absorption has a higher rate than gaseous absorption. Another reason that carbon particles have low transmittance is that carbon particles have high absorption in MWIR compared to other wavelength bands.

Weisrose *et al.* [21] studied the shielding effect of the particles on the IR signal after injecting carbon particles having the same temperature as the ambient temperature into the bypass air of a turbofan engine. First, due to the cooling of the exhaust gas by the bypass air, the IR signal was reduced by about 12% in the 4-5 μm band. Further, after injecting carbon particles into the bypass air, the IR signal was reduced by about 90%. This is because when carbon particles are injected into exhaust gas together with the bypass air, the carbon particles form an aerosol cloud, and IR signals generated in the exhaust gas plume are scattered and absorbed by the cloud, thereby shielding the IR signals.

Table 2 summarizes the approximate theoretical and experimental results obtained by Weisrose *et al.* [21]. It can be seen that the attenuation of IR intensity measured in the experiment is larger than the approximate theoretical results in all cases. Also, it was found that the error between the theoretical and experimental results increased as the angle increased.

The main reason the approximate theory predicted a smaller IR reduction than the experimental results is because of the limitations of the aerosol cloud approximation. Some important assumptions—ignoring the self-absorption of the plume and simplifying the plume as a blackbody of constant emissivity—were introduced in the approximate theory. Also, the spatial distribution pattern of the particles inside the cloud and the change in plume shape depending on the angle were not accurately taken into account in the approximate theory.

Table 2. Summary of the approximate theoretical and experimental results in Weisrose *et al.* [21].

IR Intensity Attenuation						
IR (μm)	θ = 10°		θ = 30°		θ = 90°	
	Approximate Theory	Experiment	Approximate Theory	Experiment	Approximate Theory	Experiment
2-3	89 %	95 %	86 %	92 %	68 %	85 %
3-4	80 %	96 %	78 %	82 %	56 %	75 %
4-5	87 %	98 %	65 %	94 %	48 %	94 %

2.3. A new method based on a computational solver of the full Maxwell equation

Previous studies have used approximate techniques such as aerosol cloud approximation [19,20] and Monte-Carlo method [23] to calculate the effects of the particle layer on the IR signal. However, approximate theories have several limitations, as mentioned in the previous paragraph. First, it is difficult to accurately calculate the scattering characteristics of the spatially randomly distributed pattern of the particles, and second, it is difficult to accurately calculate multiple scattering in the resonance region where the particle size is of the same order as the wavelength of IR signal. Third, they are not applicable to geometrically complicated particle layers like the one surrounding an engine plume, which is not axisymmetric.

For these reasons, to investigate the effects of a particle layer on IR signals, the present study employed a computational solver using the following full Maxwell's equations:

$$\int_{\partial\Sigma} \boldsymbol{E}\cdot d\boldsymbol{l} = -\frac{d}{dt}\iint_{\partial\Omega} \boldsymbol{B}\cdot d\boldsymbol{S}\,, \tag{9}$$

$$\int_{\partial\Sigma} \boldsymbol{H}\cdot d\boldsymbol{l} = \frac{d}{dt}\iint_{\partial\Omega} \boldsymbol{D}\cdot d\boldsymbol{S} + \iint_{\partial\Omega} \boldsymbol{J}\cdot d\boldsymbol{S}\,, \tag{10}$$

$$\iint_{\partial\Omega} \boldsymbol{D}\cdot d\boldsymbol{S} = \iiint_{\Omega} \rho d\boldsymbol{V}\,,\ \iint_{\partial\Omega} \boldsymbol{B}\cdot d\boldsymbol{S} = 0\,, \tag{11}$$

$$\iint_{\partial\Omega} \boldsymbol{J}\cdot d\boldsymbol{S} = -\frac{d}{dt}\iiint_{\Omega} \rho d\boldsymbol{V}\,. \tag{12}$$

All integrals on the left-hand side of the five equations are closed line or area integrals. Here ***E***, ***D***, ***H***, ***B***, ***J*** are the electric field intensity, the electric flux density, the magnetic field intensity, the

magnetic flux density, and the total electric current density, respectively. ρ is the total electric charge density.

The method of moments (MoM), also known as the moment method, is a powerful numerical technique for solving the electromagnetic scattering problem. The basic principle of the moment method is to convert an integral form of the full Maxwell's equation, through numerical approximations, into a matrix equation that can be solved numerically. The moment method is a full-wave solver and has the advantage of accurately calculating electromagnetic wave scattering characteristics such as scattering at the edge, diffraction, and creeping waves.

There are four basic steps in the moment method [29-33]: 1) formulate the problem in terms of an integral equation, 2) represent the unknown quantity using a set of basis functions, 3) convert the integral equation into a matrix equation using a set of testing functions, and 4) solve the matrix equation and calculate the desired quantities. They can be summarized in mathematical forms as follows,

$$L(f) = g\,, \tag{13}$$

$$f = \sum_{n=1}^{N} a_n v_n\,, \tag{14}$$

$$\sum_{n=1}^{N} a_n L(v_n) = g\,, \tag{15}$$

$$Z_{mn} a_n = b_m \text{ or } a_n = Z_{mn}^{-1} b_m\,, \tag{16}$$

$$\text{where } Z_{mn} = < v_m, L(v_n) >\,, \tag{17}$$

$$b_m = < v_m, g >\,. \tag{18}$$

Here L is a linear differential operator of the full Maxwell equation, f is the unknown function to be determined, and g is the known function representing the source. a_n are the unknown expansion coefficients. v_n are called expansion functions or basis functions. Z_{mn}, b_m are called the system matrix and the source vector, respectively [29,30].

However, since the system matrix Z_{mn} is fully populated and computationally very time consuming, so-called fast solvers were further developed to help solve the large-scale

electromagnetic wave problems, especially the scattering and radiation problems. Among various fast solvers, the multilevel fast multipole method (MLFMM) stands out for its high efficiency. The fast multipole method (FMM) was originally proposed to evaluate particle interactions and solve static integral equations rapidly. Recognizing the fact that calculating a matrix-vector product in the moment method is equivalent to calculating the mutual interaction between a set of current elements, the basic idea of FMM is first to divide the current elements into groups by their physical location in space and introduce a hub which is a collection of the current elements that are in close proximity to each other. Once the elements are connected within the same group to a single hub and the hubs are connected, the number of computations can be greatly reduced. A further gain in efficiency can be achieved by establishing another layer of hubs, leading to a multilevel method.

In the present study, FEKO's MoM-MLFMM module based on a triangular mesh was used to investigate the effects of the particle layer on electromagnetic waves in the IR band. FEKO is a general-purpose 3D electromagnetic (EM) simulator developed by Altair Engineering, derived from the German acronym meaning "field calculations involving bodies of arbitrary shape". FEKO employs the Rao-Wilton-Glisson (RWG) basis function [31], which is a linear roof-top function to calculate scattering and current at the object surface. This basis function enforces current continuity over a common edge of a triangle pair [32].

3. A multiphase flow solver for the interaction between the exhaust plume and the injected particles in flight

3.1. Compressible Navier-Stokes-Fourier equations of the multi-species gas plume

The compressible Reynolds-Average Navier-Stokes (RANS) equations including compressible and viscous effects were used to compute the thermal flow field of the multi-species gas plume in the engine nozzle [34],

$$\frac{\partial(\rho Y_i)}{\partial t}+\nabla\cdot(\rho \boldsymbol{u} Y_i)=-\nabla\cdot\boldsymbol{J}_i,\ \text{where}\ \boldsymbol{J}_i=-\left(\rho D_{i,m}+\frac{\mu_t}{Sc_t}\right)\nabla Y_i-D_{T,i}\frac{\nabla T}{T}, \tag{19}$$

$$\frac{\partial}{\partial t}(\rho \boldsymbol{u})+\nabla\cdot(\rho \boldsymbol{u}\boldsymbol{u})+\nabla p=\nabla\cdot(\boldsymbol{\tau}+\boldsymbol{\tau}_t), \tag{20}$$

$$\frac{\partial}{\partial t}(\rho h) + \nabla \cdot (\rho h \boldsymbol{u}) = \nabla \cdot \left[\left(k + k_t \right) \nabla T \right] + S_h . \tag{21}$$

Here $\rho, \boldsymbol{u}, p, T$ are the density, the velocity, the static pressure, and the temperature, respectively. The Navier-Stokes' law, Fourier's law, and Fick's law—all of which are linear—were introduced into the conservation laws of momentum, energy, and mass diffusion of species, respectively. $\boldsymbol{J}_i, Y_i$ are the mass flux and mass fraction of each species, respectively. $D_{i,m}, D_{T,i}$ are the mass diffusion coefficient for species *i* in the mixture and the thermal (Soret) diffusion coefficient, respectively. Sc_t is the turbulent Schmidt number and is defined as $\mu_t / \rho D_t$ where μ_t is the turbulent viscosity and D_t is the turbulent diffusivity. The tensors $\boldsymbol{\tau}, \boldsymbol{\tau}_t$ represent the viscous shear stress and the turbulent viscous stress, respectively. k, k_t are the thermal conductivity and the conductivity by turbulent transport, respectively. S_h represents additional heat such as radiative heat transfer.

The computational analysis was performed using the software ANSYS FLUENT, which is a density-based finite volume solver with implicit temporal integration. In order to efficiently calculate the internal and external flow fields of the engine nozzle, the *k*-*ω* SST model, which applies the *k*-*ω* model near the wall and the *k*-*ε* model for the external flow away from the wall, was used.

3.2. Multiphase model of the interaction between the exhaust plume and the injected particles in flight

The multiphase flow model can be divided into the Eulerian method and the Lagrangian method. The Eulerian method, which assumes the particle and background flow are a continuum, describes the gas-particle interaction well, but the computational efficiency and accuracy can vary greatly depending on the particle size. The Lagrangian method, on the other hand, is a method to follow the trajectories of individual particles by calculating the gas-particle interactions based on particle resistance and evaporation rate (in the case of liquid droplets). Since it calculates particles individually, the method is intuitive and the resulting algorithm is simple, but it has the disadvantage of high computational cost.

In this study, the trajectory and the behavior of the scattered particles were modeled in a Lagrangian framework using the discrete phase model (DPM) by integrating the force balance over each particle. The DPM uses the Eulerian and Lagrange methods for the gas plume of the continuous phase and the particle phase, respectively, and describes the two-way coupling between phases by calculating the mass, momentum, and energy exchange at the boundary of each phase.

The force balance equation for a moving particle in the DPM can be written as follows [34],

$$\frac{d\boldsymbol{u}_p}{dt} = F_D\left(\boldsymbol{u}-\boldsymbol{u}_p\right) + \boldsymbol{g}\frac{(\rho_p-\rho)}{\rho_p}, \tag{22}$$

where

$$F_D = \frac{18\mu}{\rho_p d_p^2}\frac{C_D\,\mathrm{Re}}{24},\ \mathrm{Re} = \frac{\rho d_p\left|\boldsymbol{u}-\boldsymbol{u}_p\right|}{\mu},\ C_D = a_1 + \frac{a_2}{\mathrm{Re}} + \frac{a_3}{\mathrm{Re}^2}. \tag{23}$$

Here $\boldsymbol{u}$ is the velocity, ρ is the density, μ is the viscosity of the fluid, and d is the particle diameter. F_D is the drag force per unit mass, and C_D is the drag coefficient of a particle with a spherical shape. The subscript p represents the property of the particle. $\boldsymbol{g}$ is the gravitational acceleration vector, and Re is the Reynolds number based on the relative velocity between the fluid and the particle. a_1, a_2, and a_3 are constants for smooth spherical particles that apply over wide ranges of Reynolds number.

When injected water droplets are placed in a hot exhaust plume flow, evaporation occurs at the droplet surface. In this case, the decrease in the mass of the water droplet m_p —that is, the evaporation rate—can be expressed as follows,

$$\frac{dm_p}{dt} = -N_i A_p M_{w_i}, \tag{24}$$

where A_p, M_{w_i} are the surface area of the droplet and the molecular weight of species i, respectively. N_i is the molar flux of the vapor and can be expressed as follows,

$$N_i = k_c\left(C_{i,s} - C_{i,\infty}\right), \tag{25}$$

where k_c is the mass transfer coefficient. $C_{i,s}$, $C_{i,\infty}$ are the vapor concentrations at the droplet surface and in the bulk gas (plume), respectively, and are defined as follows,

$$C_{i,s} = \frac{p_{sat}\left(T_p\right)}{RT_p},\ C_{i,\infty} = \frac{X_i p}{RT_\infty}, \tag{26}$$

where p_{sat} is the saturated vapor pressure, T_p is the droplet temperature, R is the universal gas constant, X_i is the bulk mole fraction of species i, and T_∞ is the bulk temperature in the gas. When Eqs. (24)-(27) are combined, an interesting relation which can reveal the strong dependence of the radius of the droplet on the droplet temperature and the bulk gas temperature can be derived:

$$\frac{dr_p}{dt} = -\frac{1}{\rho_p} N_i M_{w_i} = \mathrm{fn}(T_p, T_\infty). \tag{27}$$

In addition, the change in the droplet temperature can be calculated based on the heat balance, that relates the sensible heat change in the droplet to the convective and latent heat transfer between the droplet and the continuous gas phase:

$$m_p c_p \frac{dT_p}{dt} = hA_p\left(T_\infty - T_p\right) - \frac{dm_p}{dt} h_{fg} + A_p \varepsilon_p \sigma\left(\theta_R^4 - T_p^4\right). \tag{28}$$

where c_p is the droplet heat capacity, h is the convective heat transfer coefficient, h_{fg} is the latent heat, ε_p is the dimensionless particle emissivity, σ is the Stefan-Boltzmann constant, and θ_R is the radiation temperature. The three terms on the right-hand side represent the convective heat transfer, heat transfer associated with vaporization, and radiation heat transfer, respectively.

3.3. Validation of the DPM multiphase model

To validate the DPM multiphase model, a multiphase flow analysis was performed for an experimental work, involving the interaction of a rocket exhaust plume and liquid water droplet conducted by Yi *et al*. [35]. They injected water droplets around the exhaust plume of a rocket motor generating temperatures of up to 3,000 K, as illustrated in Fig. 3, and then analyzed the cooling effect of water mist on the exhaust plume. A 50 μm diameter water droplet with a temperature of 288.15 K was injected at a speed of 25 m/s and a mass flow rate of 1.8 kg/s. A temperature measurement system was installed at 0.1 m intervals at a distance of 1.75 m from the rocket motor exit (points 1-4). The rocket motor generated exhaust gas at a pressure of 7 MPa and a temperature of 3,000 K from the nozzle inlet. The background state was selected to have a pressure of 101,325 Pa and a temperature of 300 K as in the experiment. While Yi *et al*. [35] used the RNG k-ε turbulence model and the mixture multiphase flow model, the present study used the

k-ω SST turbulence model and the DPM. In addition, the number of computational grids was significantly increased in the region where the exhaust gas plume and particles are mixed.

The computational grid used to validate the DPM multiphase model in the present CFD simulation is shown in Fig. 3. Table 3 shows the comparison of the experimental and computational temperature at points 1-4. There was a difference of about 3.5% or less at all points, confirming that the present DPM multiphase model can describe the interaction between the plume and droplets fairly well.

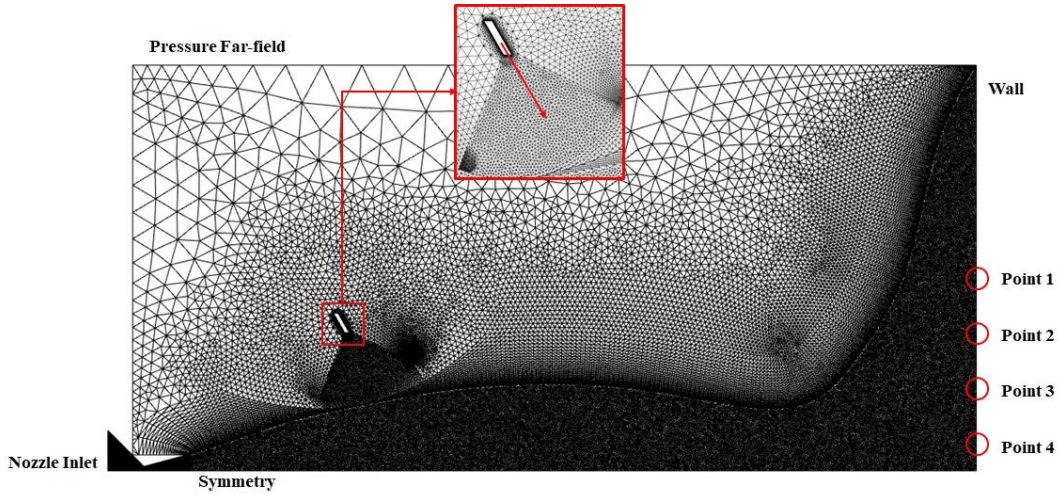

Fig. 3. Computational grid system for validation of DPM.

Table 3. Comparison of experimental and CFD results.

	Point 1	**Point 2**	**Point 3**	**Point 4**
Experiment (K)	402	410	415	422
CFD Result (K)	387.92	398.34	408.81	413.12
Relative Error (%)	3.50	2.84	1.49	2.10

3.4. Geometries and boundary conditions of the CFD computation for the engine exhaust plume

Figure 4 shows the modeling of an axisymmetric nozzle and the particle injection system. The nozzle length was set to 0.83 times the nozzle inlet diameter, and the nozzle outlet diameter to 0.69 times the inlet diameter. The injector was oriented parallel to the exhaust gas plume to minimize the thrust loss of the nozzle. Eight injectors were placed at a distance equivalent to the

diameter of the nozzle from the nozzle exit so that the injected particles could shield the exhaust gas plume.

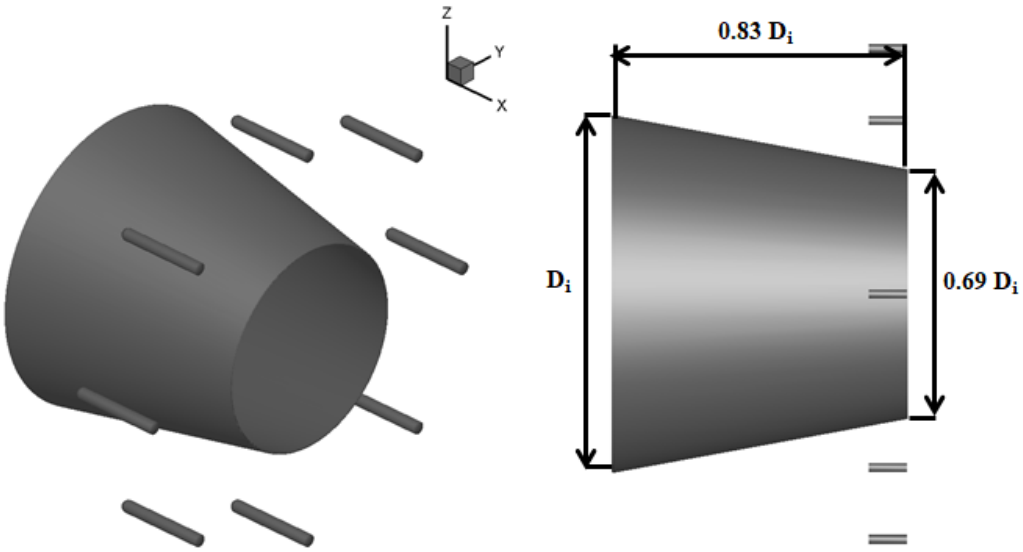

Fig. 4. Geometries of nozzle and injectors.

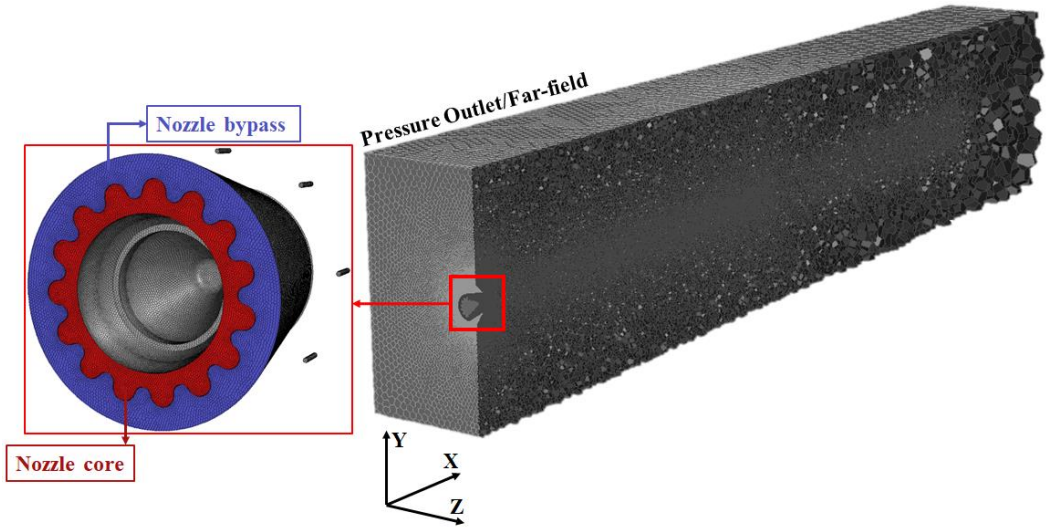

Fig. 5. Computational grid system and boundary conditions.

The flow field was discretized using 7.1 million polyhedral grids. In order to further improve the accuracy of the analysis, more grids were placed in the exhaust gas and particle injection areas, as shown in Fig. 5.

Table 4 summarizes the flow and particle injection conditions for a cruise flight condition. The altitude and speed of the cruise flight condition were obtained for the situations a UCAV may

encounter when approaching or moving away from targets defended by air-to-air missile (AAM) and surface-to-air missile (SAM). Atmospheric conditions were based on the international standard atmosphere model. The ground condition represents the maximum thrust condition in a ground stationary state, and it was simulated using the pressure outlet in the simulation. The cruising condition represents a flight condition of Mach number 0.7 at an altitude of 20,000 ft, and it was simulated using the pressure far-field. The mole fraction of engine exhaust gas was obtained assuming complete combustion. The exhaust gas and bypass air external flows were assumed to consist of CO_2 13%, H_2O 13%, N_2 74%, and O_2 21%, N_2 79%, respectively.

Table 4. Boundary conditions for ground and cruise flight conditions.

		Ground (0 ft)	Cruise (20,000 ft)
Free-stream (Pressure Outlet/Far-field)	**Pressure (pa)**	101,352.58	46,563.26
	Temperature (K)	288.15	248.56
	Mach	0.0	0.7
Nozzle Core (Mass Flow Inlet)	**Pressure (pa)**	146,375.0	88,625.21
	Temperature (K)	811.83	798.04
	Mass Flow Rate (kg/s)	5.28	3.47
Nozzle Bypass (Mass Flow Inlet)	**Pressure (pa)**	150,305.0	94,602.96
	Temperature (K)	334.34	321.31
	Mass Flow Rate (kg/s)	15.2	10.51
Particle (DPM)	**Mass Flow Rate (kg/s)**	1.025	0.7
	Temperature (K)	288.15	266.73
	Particle Diameter (μm)	5, 10	10
	Time (sec)	0~5	0~5
	Material	H_2O, Carbon	H_2O, Carbon
Wall		No-slip, adiabatic	

In order to prevent flow instability in the exhaust gas due to particle injection, a particle injection flow rate of 5% was selected. In a recent previous study [28], it was found that when the particle injection flow rate increased over a certain level, the plume flow which has a different density strongly interacts with the particles, resulting in a Kelvin-Helmholtz instability, which quickly turns into an asymmetric plume configuration. The selected particle sizes were 5 and 10 μm diameters, similar to the wavelength in the IR band, and the particles were injected for 5 seconds. To investigate the effect of the type of particle materials on the IR characteristics, two types of particles (liquid water droplets and solid carbon particles) were considered.

4. Effects of particle layer on thermal flow and IR characteristics

4.1 Effects of particle layer on thermal flow characteristics using the DPM multiphase solver

First, the thermal flow field of the exhaust gas plume was analyzed for ground and cruise flight conditions by changing the size and type of injection particles. When water droplets with a diameter of 5 μm were injected in a ground stationary state, vaporization occurred immediately due to the high temperature exhaust gas. The smaller the particles, the faster the vaporization occurred, so the water particles could not completely cover the exhaust gas plume.

On the other hand, the solid carbon particles did not undergo a phase change and maintained their size, so that all of the exhaust gas plume could be shielded.

The thermal flow field for the ground condition was also analyzed using particles with an enlarged diameter of 10 μm, as summarized in Figs. 6, 7. Fig. 6 (a) shows the thermal flow field when no particles were injected, while Fig. 6 (b) and (c) show the case where water droplets and carbon particles were injected, respectively. The liquid water droplets decreased in diameter due to vaporization, while the solid carbon particles retained their size. In both cases, flow instability did not occur in the exhaust gas plume, because the injection flow rate and particle size were not so large. The temperature of water droplet and carbon particles was 286 K at the nozzle exit, and as the flow moved downward, the temperature increased due to heat transfer with the hot plume, reaching a maximum of 308 K and 342 K locally, respectively. Therefore, it can be said that the IR radiation from the surface of particles is insignificant compared to the IR radiation from the high temperature nozzle surface or plume.

Figure 7 shows that for the temperature reduction effect, water was superior to carbon and reduced the length of the plume by up to 4.5%.

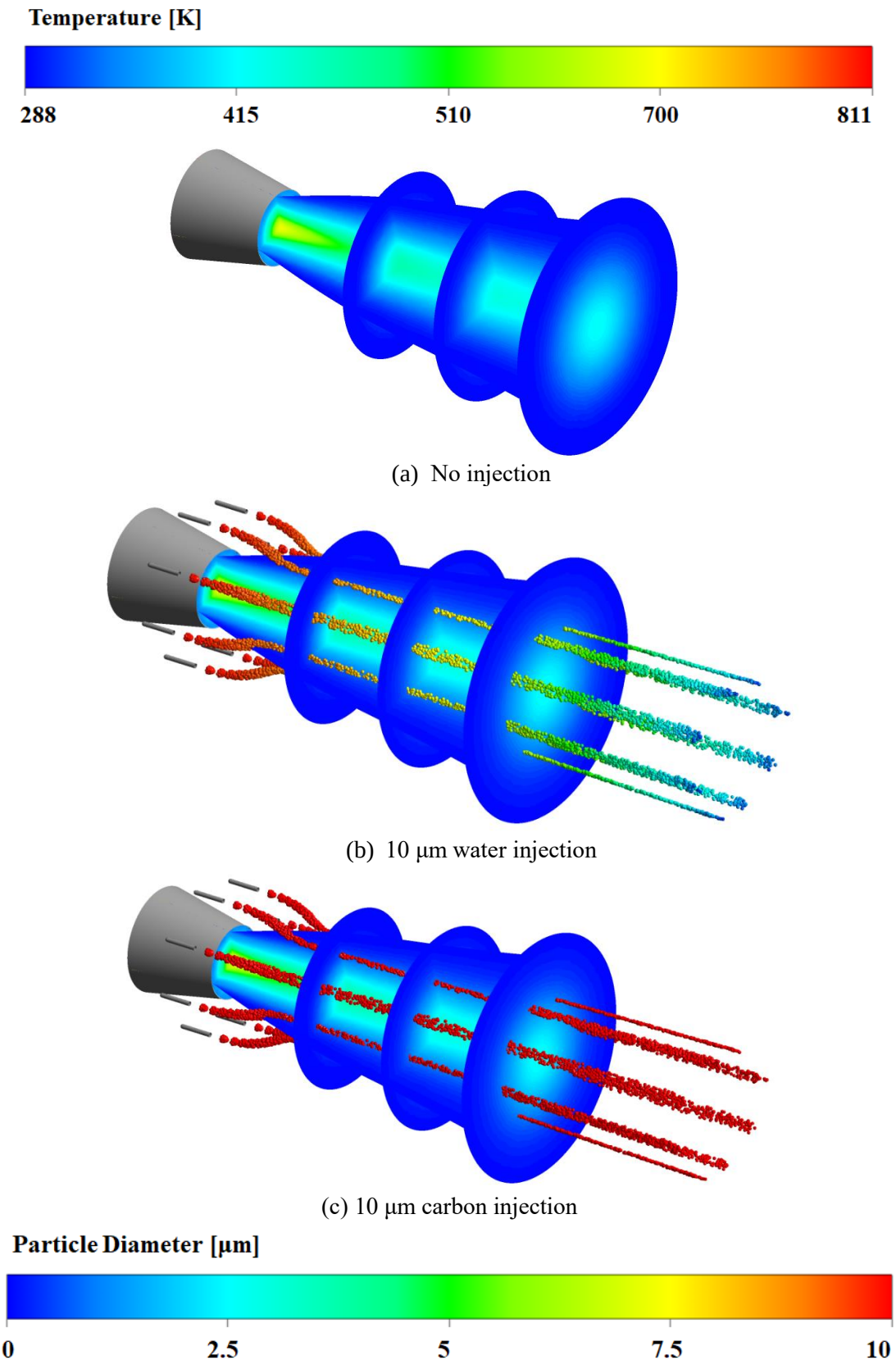

Fig. 6. Temperature contour and particle diameter distribution for ground condition for an injected particle diameter of 10µm.

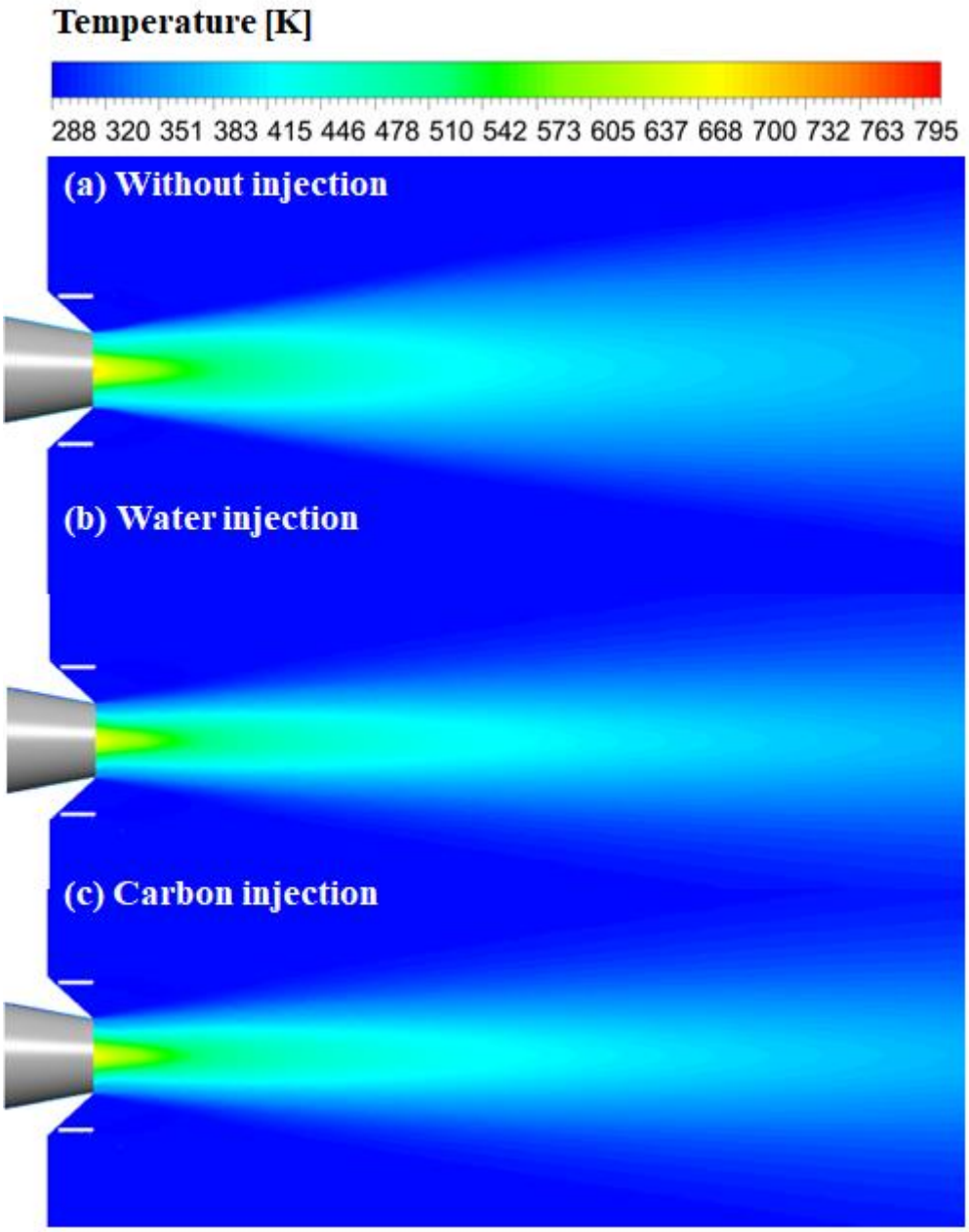

Fig. 7. Temperature reduction effect under ground condition with 10 μm particle injection.

Figure 8 shows the particle diameter and concentration distribution on the streamlines emanating from the tip of the injector. When particles with a diameter of 5 μm were injected, all of the water droplets were vaporized after moving about 1 m, as shown in Fig. 8 (a). In contrast, solid carbon particles did not change in diameter. This is because the average temperature at the outlet of the nozzle is about 500 K, which is far below the sublimation temperature of carbon (3,000 K), so that sublimation does not occur. Particle concentration was higher near the injector, and decreased as it moved downstream. That is, a high concentration is maintained near the

injector because many particles are concentrated in a narrow area, whereas the concentration decreases because the injected particles are diffused as the flow moves downstream. Because the carbon particles did not change in diameter, their change in concentration was less than that of water droplets, except near the nozzle outlet (within 1m) where the particles were rapidly diffused.

Figs. 8(a) and (b) show the effect of the size of water droplets. It can be seen that the 10 μm particle moves about 1.8 times further than the 5 μm particle. This indicates that the degree of exhaust gas flow shielding by the particle layer is quite sensitive to particle size in the case of water droplets. Interestingly, Fig. 8(c) for the cruise flight condition shows that water droplets hardly vaporize, unlike the ground condition. This is because the air temperature is very low compared to the ground condition, and the flight speed is high. Moreover, due to the increase in flight speed and the decrease in the temperature of the air and bypass flow, the exhaust gas is more rapidly cooled by mixing with the atmosphere than in the ground condition, and as a result, the exhaust gas was 54% shorter in length compared to the ground condition. In addition, due to the high air flow velocity, the particles did not mix with the exhaust gas and move along the air flow, so that heat transfer from the exhaust gas to the particles was small compared to the ground condition. As a result, the diameter of the water droplets was reduced to a lesser extent, allowing more exhaust gas shielding.

The shielding of the IR signal of exhaust gas by injecting particles is effective even in the case of the engine's wet mode. However, in the case of water injection, it is necessary to significantly increase the injection amount to shield the IR signal due to an increase in exhaust gas temperature.

On the other hand, in both dry and wet modes, the change in thrust due to particle injection was found to be insignificant at about 0.1%.

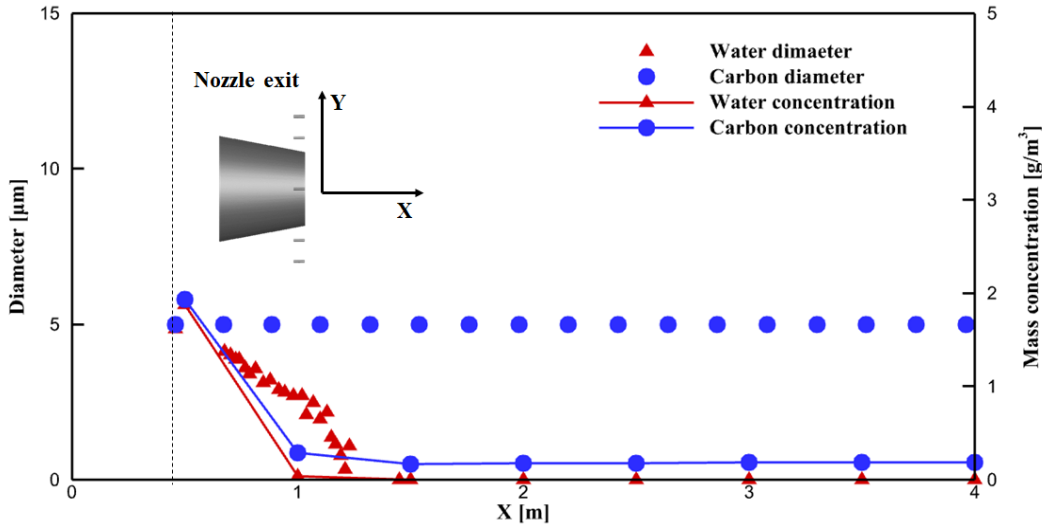

(a) 5μm particle injection under ground condition

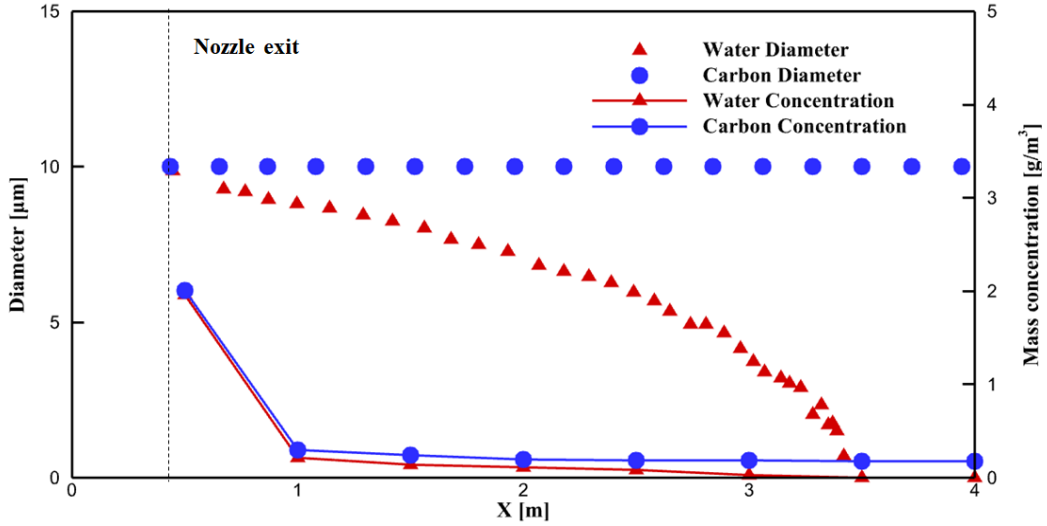

(b) 10μm particle injection under ground condition

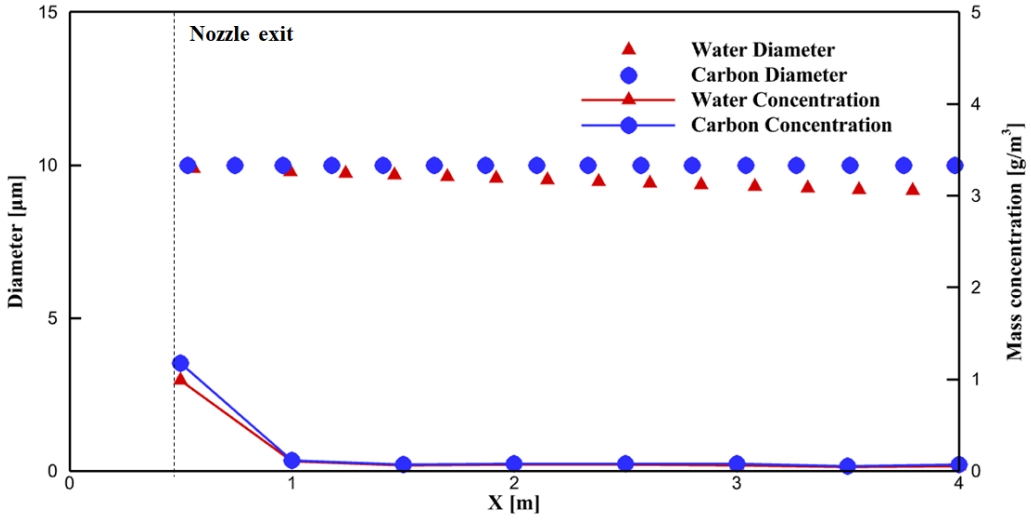

(c) 10 μm particle injection under cruise condition

Fig. 8. Particle diameter and mass concentration in the nozzle axis direction.

4.2. Effects of particle layer on IR transmission using a computational solver of the full Maxwell equation

After calculating the particle diameter and concentration distribution using the DPM multiphase solver, the number of particles per unit volume (N) and the spacing between neighboring particles (L_S) can be determined with the following relations [36],

$$N = \frac{6c_p}{\pi d_p^3 \rho_p},\ L_S = \sqrt[3]{\frac{1}{N}}, \tag{29}$$

where d_p is the diameter of the particle, c_p is the particle concentration (kg/m^3), and ρ_p is the density of the material constituting the particle.

Using the information on the number of particles and the inter-particle distance, the computational domain can be defined for the particle layer shielding the exhaust plume to which the full Maxwell solver (MLFMM) will be applied. Particles are randomly placed within the domain, and the spacing between particle centers is determined using the same constraint as the particle diameter to prevent overlapping of the particles. The diameter of the particle was kept constant, and the sphere was located by selecting the coordinates on the XY plane randomly. An example of the randomly placed particle distribution pattern is shown in Fig. 9.

While keeping the total particle mass constant, the transmittance of the particle layer was calculated using the MLFMM solver by varying the particle diameter and material type. In Fig. 9, the X, Y, and Z represent the axial direction of the nozzle exhaust plume, the radial direction from the center of the plume, and the circumferential direction relative to the nozzle axis, respectively. It is assumed that the electromagnetic wave in the IR band propagates in the radial direction from the center of the plume, and the electromagnetic wave is incident in the +Y direction. Since the density of a water droplet is half that of carbon particle, the number of water droplets for the same mass is twice that of carbon particles. If the diameter of a particle is doubled, the number of particles must be reduced by 1/8 to maintain the same mass. Table 5 summarizes the triangular mesh size used to cover the surfaces of particles and the electromagnetic properties of the particles used to calculate the electromagnetic wave scattering by particles [37-39].

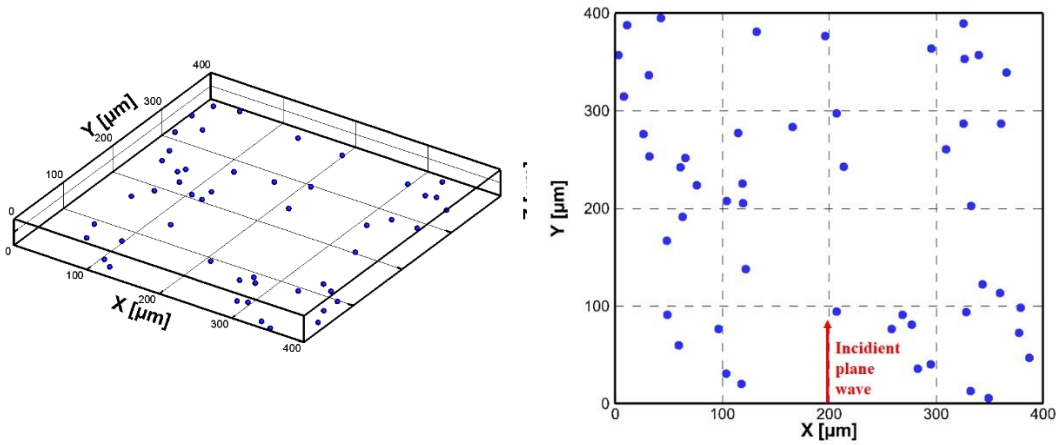

(a) Isometric view (b) Top view

Fig. 9. Randomly placed configuration of particles.

Table 5. Computational mesh size and electromagnetic properties of particles.

	Water	Carbon
Mesh Size	$\lambda/12$	
Relative Permittivity	1.778	7.207
Loss Tangent	0.0156	0.8352
Impedance (Ω)	288.37	140.16

Figure 10 shows the contour of the transmission by scattering and absorption when electromagnetic waves of 4.4 μm wavelength were incident on a particle layer composed of 5 μm-sized water droplets and carbon particles. The contour shown in Fig. 10 (a) was calculated from the mid-section in the Z direction. Since the total mass is kept constant, water with a lower density has more droplets, and as a result, there are more regions where scattering or absorption occurs. However, for carbon particles with a high loss tangent, the absorption effect of unit particles is much greater than that of water droplets, so the transmittance is reduced [19].

When the case where particles were independently located far away from neighboring particles was compared with the case where several particles were aggregated, a significant difference in the transmission distribution around the particle was found. That is, when two or more particles are located close to each other in a direction parallel or perpendicular to the incident electromagnetic wave, the transmission value is further reduced, compared to an independent single particle. This can be confirmed from the contour around the three particles located parallel

to the electromagnetic wave at the right side of Fig. 10 (b). (The reduction in transmission is most noticeable in the third particle). This can be attributed to the complex nonlinear resonance phenomenon that occurs when the particle size and the wavelength of the incident electromagnetic wave are similar.

To examine the scattering and absorption effects of individual particles in more detail, the electric field distribution around a single particle was calculated. Figure 11 shows the contour of the electric field formed by scattering and absorption when an electromagnetic wave of 100 V/m with a 4.4 μm wavelength was incident on a single water droplet and a carbon particle with a size of 5 μm. A significant amount of forward scattering occurred in the water droplets and reached up to 2.4 times the incident wave. On the other hand, carbon particles have a very weak electric field inside and around the particles due to their high loss tangent.

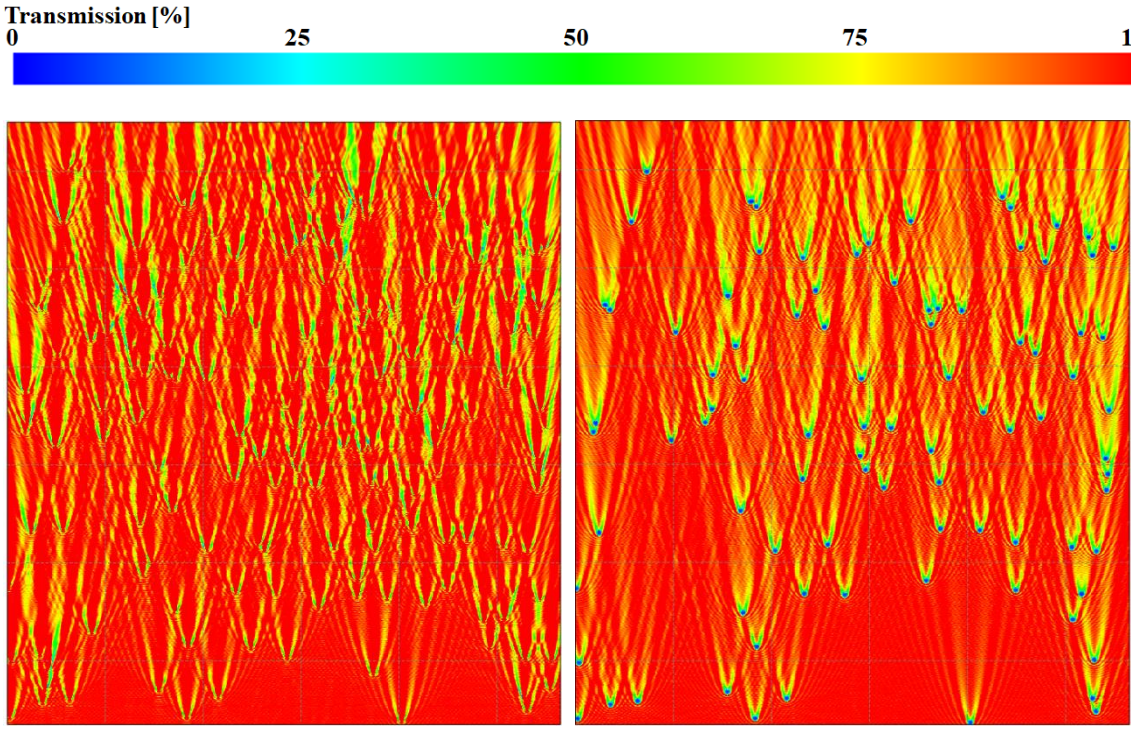

(a) Water droplet (b) Carbon particle

Fig. 10. Electromagnetic field contour at a wavelength of 4.4 μm for 5 μm diameter particles.

This trend is detailed in Fig. 12, which plots the electric field distribution for a line parallel to the incident wave crossing the particle center, and a line perpendicular to the incident wave behind the particle. It can be seen from Fig. 12 (a) that the water droplet has a greater electric field strength

than both inside and behind the carbon particle. In particular, a near-zero electric field strength formed inside the carbon particles, while the electric field increased in the direction of the electromagnetic wave inside the water droplets. Fig. 12 (b) confirms that the same trend appears at the rear of the particle.

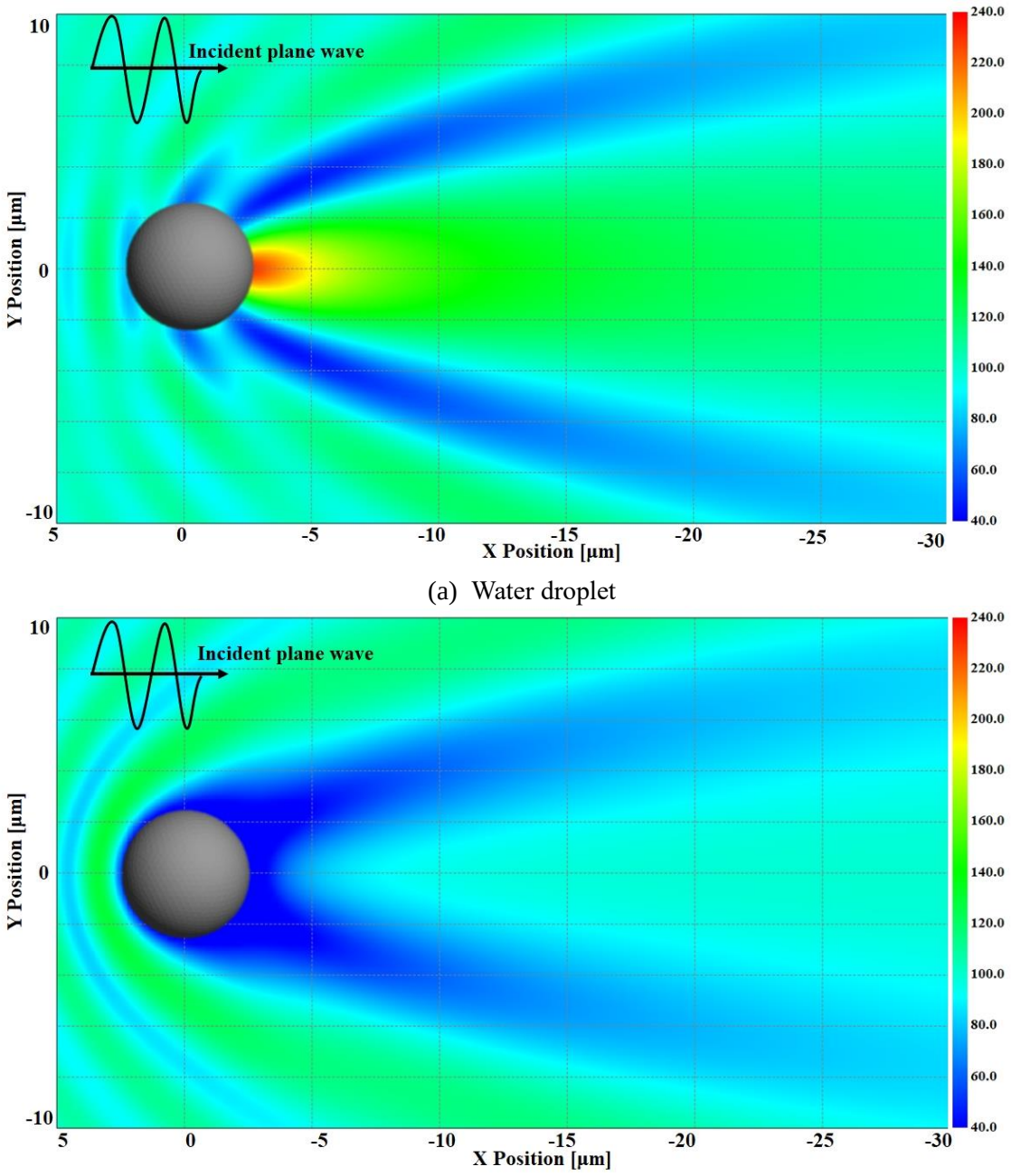

(a) Water droplet

(b) Carbon particle

Fig. 11. Contour of electric field for with 5 μm diameter water droplet and carbon particle.

Meanwhile, the electromagnetic wave scattering properties of water droplets and carbon particles were greatly affected by the difference in impedance (η) at the particle surface. The

degree of reflection that occurs when electromagnetic waves pass through different media is determined by the difference in impedance (that is, the reflection ratio, $|\Delta\eta|/\overline{\eta}$). From Table 5, the reflection ratio is 0.1417 at the air (377 Ω) − water (288 Ω) interface, and 0.458 at the air (377 Ω) − carbon (140 Ω) interface. From this, the carbon particles reflect more electromagnetic waves from the front part of the particles compared to water droplets. This trend can be seen in Figs. 11 and 12. In summary, all other conditions being equal, carbon particles reflect more and absorb more than water droplets, resulting in a higher shielding effect, at least at this wavelength.

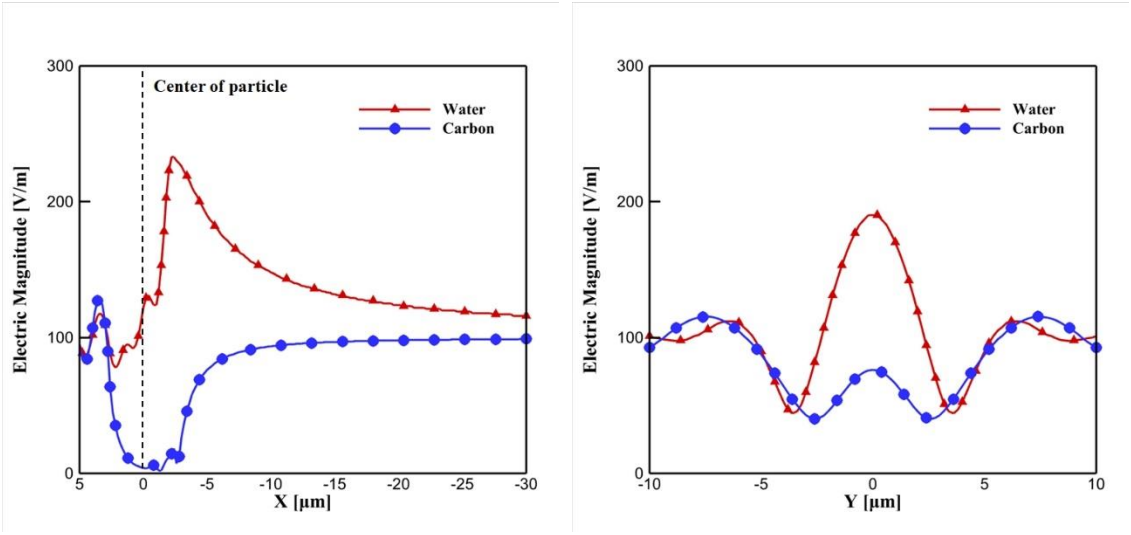

(a) -30 μm ≤ X ≤ 5 μm , Y=0 μm (b) X= -5 μm, -10 μm ≤ Y ≤ 10 μm

Fig. 12. Electric field distribution for a line parallel to the incident wave crossing the particle center, and a line perpendicular to the incident wave behind the particle (5 μm particle).

In order to examine the effects of the loss tangent on scattering and absorption, the loss tangent value was increased and calculated for a single particle. Figure 13 shows the change in the electric field that occurs when the loss tangent value of a 5 μm particle increases. As the value of the loss tangent increased, the strength of the electric field inside and behind the particle decreased, and when the loss tangent reached 1.0, it was significantly reduced to less than 1/4 of the incident electric field. Figure 14 shows the electric field strength for varying Y positions at the X=0 μm position on the line perpendicular to the incident wave crossing the particle center. When the loss tangent increased in the order of 0.5 and 1.0, the strength of the electric field decreased to less than 1/2 and 1/4 of the incident electromagnetic wave.

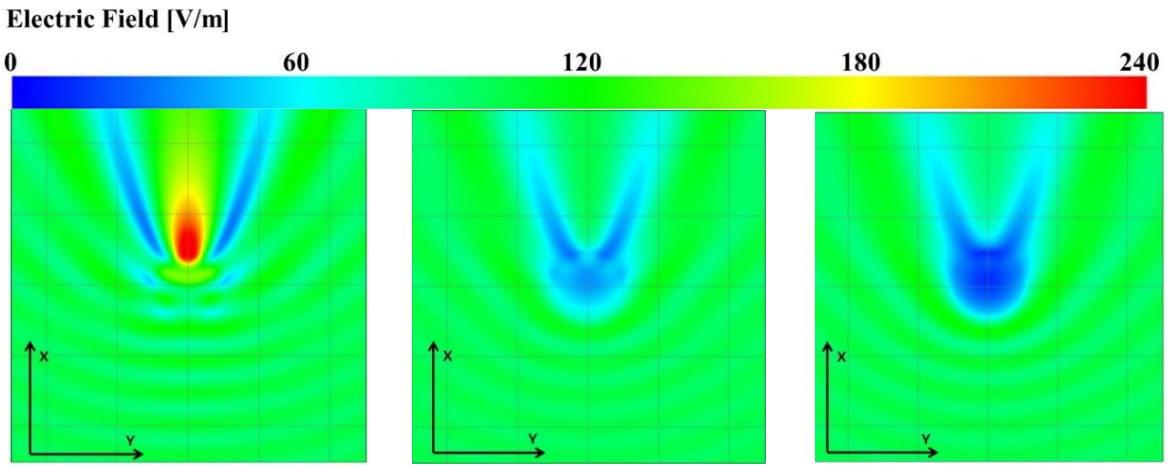

(a) Loss tangent : 0.0 (b) Loss tangent : 0.5 (c) Loss tangent : 1.0

Fig. 13. Comparison of electric fields for different values of loss tangent (5 μm particle).

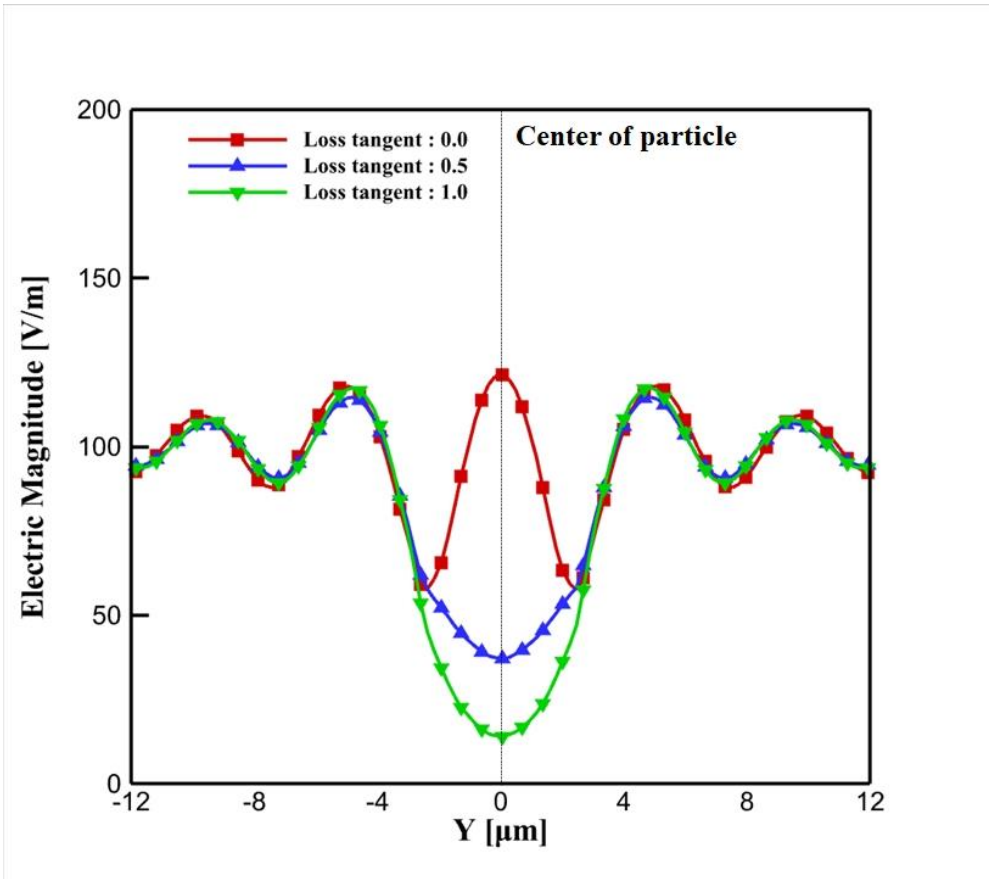

Fig. 14. Electric field distribution for varying Y positions at the X=0 μm position (5 μm particle).

Next, the scattering and absorption effects were calculated for a particle size of 10 μm while the total mass was kept constant. In the case of water droplets, since vaporization occurs, the larger the size, better it can shield the engine exhaust gas plume. As was done in Fig. 9, particles were

randomly placed within the domain, and the spacing between particle centers was selected such that the average distance between particles was 5 d_p. Compared to the case with a particle size of 5 μm in Fig. 10, the number of particles decreased by 1/8 when the particle size increased by 2 times. As the number of particles decreased, the transmittance increased and the shielding effect provided by the particles decreased. This point can be confirmed in Fig. 15, which shows the contour of the transmission by scattering and absorption of a particle layer composed of 10 μm-sized water droplets and carbon particles. Since the number of particles is significantly reduced compared to the case with 5 μm size, the total transmittance will depend on the scattering and absorption characteristics of the individual particles.

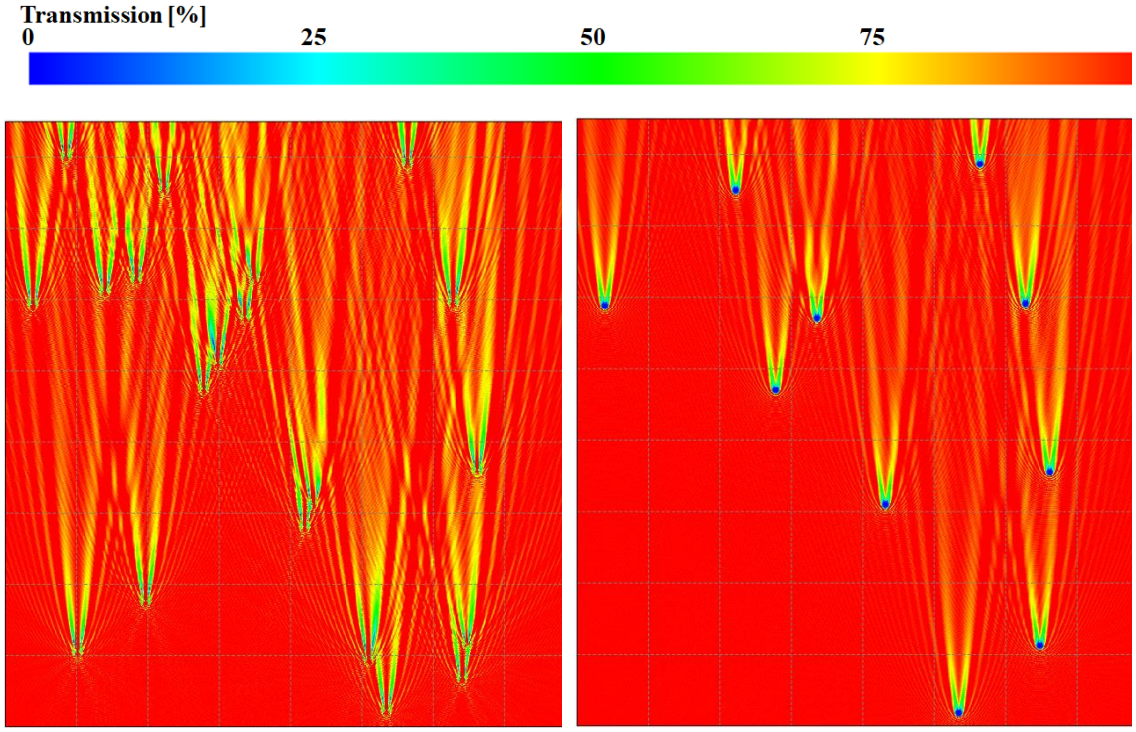

(a) Water droplet (b) Carbon particle

Fig. 15. Electromagnetic field contour at 4.4 μm wavelength for particles with 10 μm diameter.

To investigate the scattering and absorption effects of individual particles, the electric field distribution around a single particle was calculated. Figure 16 shows the contour of the electric field formed by the scattering and absorption of a single water droplet and a carbon particle with a size of 10 μm. Qualitatively, it shows the same results as in Fig. 11 for the 5 μm-sized particles. That is, the water particles show forward scattering up to 4 times the incident wave, whereas

carbon particles have a very weak electric field inside and around the particles due to the high loss tangent. This trend can be confirmed in Fig. 17, which shows the electric field distribution on a line parallel to the incident wave crossing the particle center, and a line perpendicular to the incident wave behind the particle.

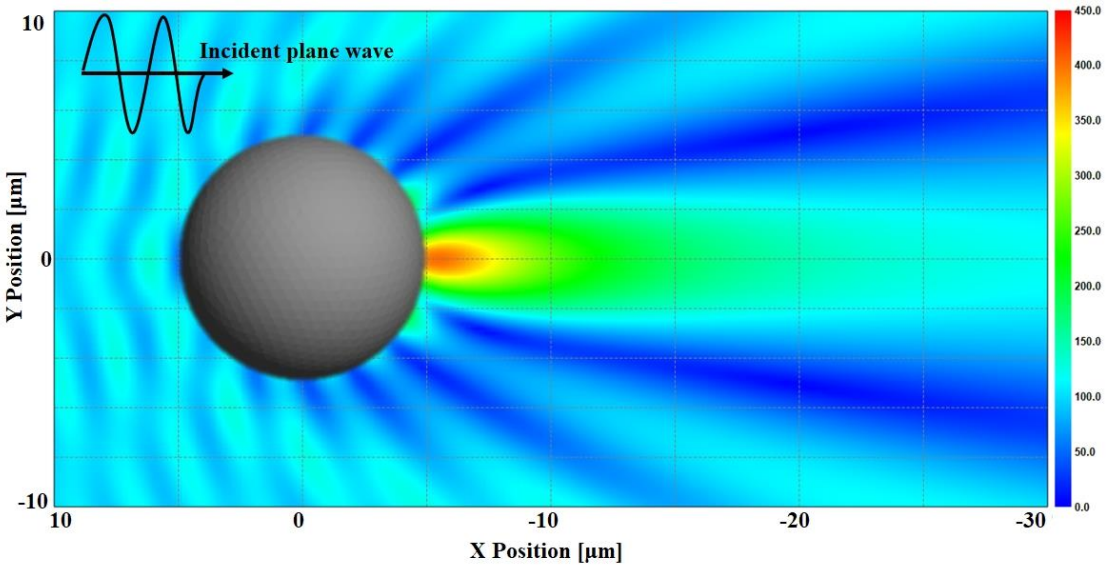

(a) Water droplet

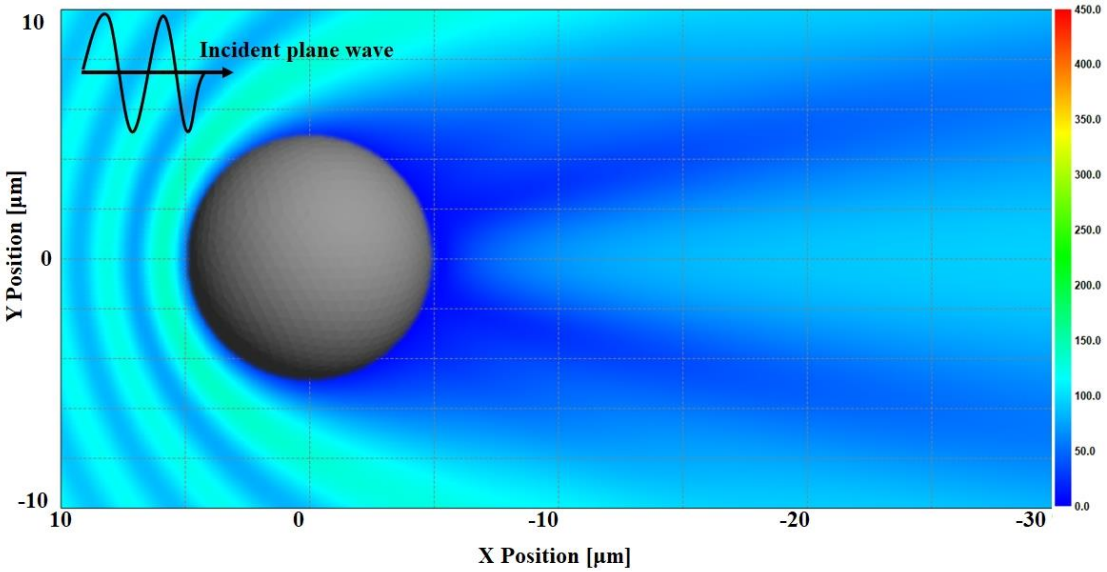

(b) Carbon particle

Fig. 16. Contour of electric field for a water droplet and a carbon particle 10 µm in diameter.

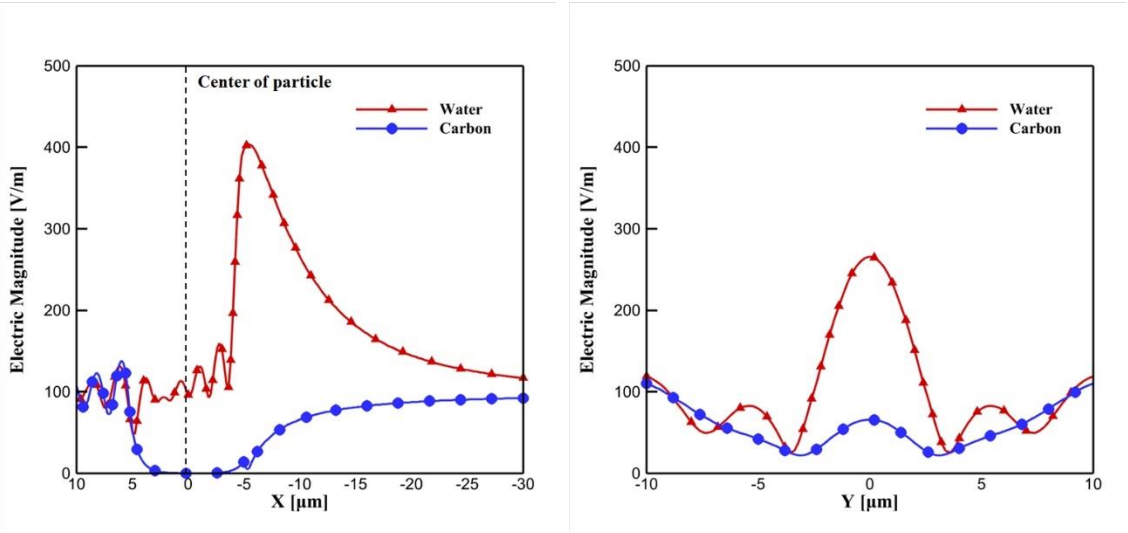

(a) -30 μm ≤ X ≤ 10 μm, Y = 0 μm (b) X= -10 μm, -10 μm ≤ Y ≤ 10 μm

Fig. 17. Electric field distribution for a line parallel to the incident wave crossing the particle center and a line perpendicular to the incident wave behind the particle (10 μm particle).

Finally, the transmittance of the particle layer composed of water droplets and carbon particles was analyzed for a wavelength of 3~5 μm. Particles with diameters of 5 and 10 μm were randomly placed in a space of 0.32 mm^2 (case 1) and 0.64 mm^2 (case 2), while maintaining the same total mass. It can be noted that the shielding effectiveness of case 1 is higher than that of case 2, because case 1 has a higher particle density than case 2. Some conclusions can be drawn from Fig. 18.

First, solid carbon particles exhibit little change in transmittance with respect to wavelength, and a large number of particles is better at reducing transmittance. For water droplets, the 10 μm-sized particles showed little change in transmittance with respect to wavelength, while the 5 μm-sized particles showed increased transmittance with increasing wavelength. Interestingly, this observation of increasing transmittance with increasing wavelength is consistent with the results of Dai *et al*. [40] for 5 μm-sized particles.

In the case of water droplets, the shielding effectiveness of 5 μm or 10 μm size particles was different depending on whether the wavelength of the incident IR signal was smaller or larger than 3.5~3.7 μm. That is, a large number of 5 μm particles were more effective for shielding at wavelength bands smaller than 3.5~3.7 μm, but 10 μm particles were better for shielding at wavelength bands larger than 3.5~3.7 μm. For water droplets, where scattering and reflection play

a more important role than absorption, this complex result is thought to be caused by the high nonlinearity typical of the resonant region, where the wavelength and particle size are similar.

The IR reduction effect can be analyzed in terms of optical blocking, absorption, and temperature reduction. Optical blocking and absorption effects can be analyzed by considering hypothetical perfect electrical conductor (PEC) and perfect absorption material (PAM) particles, respectively. In the case of 4.4 μm wavelength, the shielding effectiveness increased in the order of water, PEC, and PAM for particles with the specific weight of water, and in the order of PEC, PAM, and carbon for particles with the specific weight of carbon.

In the present results, which were obtained under the condition that the total mass remained the same, 5 μm water droplets in wavelength bands below 3.5~3.7 μm, and 10 μm water droplets or 5 μm carbon particles in wavelength bands above 3.5~3.7 μm turned out to be more effective for shielding.

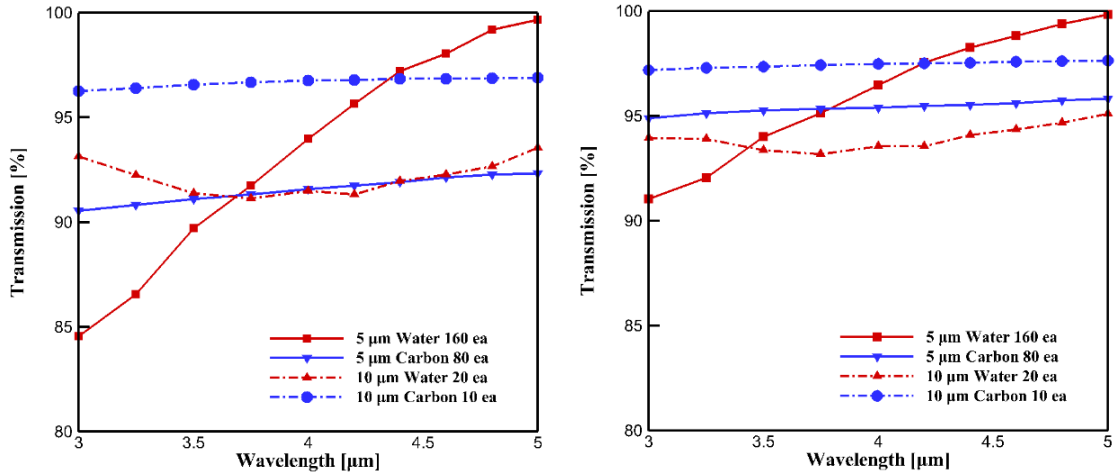

(a) Case 1 (0.32 mm^2) (b) Case 2 (0.64 mm^2)

Fig. 18. Transmission for different particle injecting conditions.

5. Conclusions

In this study, an active IR reduction technique was investigated that creates a particle layer surrounding the engine exhaust gas plume, to reduce the infrared signal caused by the hot part inside the nozzle and the nozzle gas plume. A Eulerian-Lagrangian-based DPM multiphase method was used to calculate the multiphase flow, composed of exhaust gas and particles

introduced by injection. Water droplets and carbon particles with diameters of 5 and 10 μm were considered. Both particles have different phase change properties in the engine exhaust at high temperatures, and as a result, showed a complex pattern of infrared signal reduction during flight.

In cruise flight conditions, the temperature of the bypass air was low due to the low air temperature, and the exhaust gas was actively mixed with the atmosphere due to the high speed. As a result, the engine exhaust gas plume cooled rapidly, and the length of the exhaust gas was shortened by about half compared to the ground condition. In cruise flight conditions, less water droplets vaporized, and the concentrations of water droplets and carbon particles remained similar, shielding the exhaust gas plume by more than 5 m in both cases.

After calculating the particle diameter and concentration distribution using the DPM multiphase solver, the number of particles per unit volume and the spacing between neighboring particles were determined. Particles were randomly placed within the particle layer while keeping the total particle mass constant. To analyze the shielding effect according to particle size, material type, and distribution pattern, the transmittance of IR electromagnetic waves with wavelengths of 3~5 μm were analyzed using a full Maxwell multi-level fast multipole method.

When the total mass was kept the same, 5 μm water droplets in wavelength bands below 3.5~3.7 μm, and 10 μm water droplets or 5 μm carbon particles in wavelength bands above 3.5~3.7 μm were more effective for shielding. If the single layer transmittance information obtained in the present study is extended to actual particle layers of several tens of centimeters, it is expected that the observed shielding effect will be significantly higher.

The shielding effectiveness of solid particle injection increases when the particle diameter is similar to the size of the wavelength. However, considering the substantial change in the flow field due to liquid droplet injection, small-sized water droplets evaporate quickly, which reduces the shielding effectiveness. Therefore, for effective shielding, both the change in droplet diameter due to interaction with the exhaust gas and the wavelength of the infrared signal must be taken into account. In addition, when estimating the total radiance received by a sensor to evaluate the overall benefit of particle shielding, not only transmission but also plume radiation must be considered.

In a future study, using the techniques developed here, we plan to calculate the optimal

injection conditions considering the amount, size, and type of particles per each position of the particle layer around the engine exhaust gas plume in flight, when local mass distribution is not constant.

Acknowledgement

This work was supported by the Aerospace Low Observable Technology Laboratory Program of the Defense Acquisition Program Administration and the Agency for Defense Development of the Republic of Korea. The authors thank the referees of this paper for their valuable and very helpful comments and suggestions.

Reference

[1] J.R. White, *Aircraft Infrared Principles, Signatures, Threats, and Countermeasures*, Naval Air Warfare Center Weapons DIV, Chinal Lake CA, 2012. https://doi.org/10.21236/ada566304

[2] X. Sun, Z. Wang, L. Zhou, J. Shi, and Z. Liu, "Experimental and computational investigation of double serpentine nozzle," *Journal of Aerospace Engineering*, Vol. 229, No. 11, pp. 2035-2050, 2015. https://doi.org/10.1177/0954410014564402

[3] C.H. An, D.W. Kang, S.T. Baek, and R.S. Myong, "Analysis of plume infrared signatures of S-shaped nozzle configurations of aerial vehicle," *Journal of Aircraft*, Vol. 53, No. 6, pp. 1768-1778, 2016. https://doi.org/10.2514/1.C033685

[4] N. Baranwal and S.P. Mahulikar, "IR signature study of aircraft engine for variation in nozzle exit area," *Infrared Physics & Technology*, Vol. 74, pp. 21-27, 2016. https://doi.org/10.1016/j.infrared.2015.11.001

[5] N. Baranwal and S.P. Mahulikar, "Review of Infrared signature suppression systems using optical blocking method," *Defence Technology*, Vol. 15, No. 3, pp. 432-439, 2016. https://doi.org/10.1016/j.dt.2018.12.002

[6] S.P. Mahulikar, P. Rastogi, and A. Bhatt, "Aircraft signature studies using infrared cross section and infrared solid angle," *Journal of Aircraft*, Vol. 59. No. 1, pp. 12-136, 2021. https://doi.org/10.2514/1.C036370

[7] Y. Shan, X. Zhou, X. Tan, J. Zhang, and Y. Wu, "Parametric design method and performance analysis of double S-shaped nozzles," *International Journal of Aerospace*, Vol. 2019, pp. 1-24, 2019. https://doi.org/10.1155/2019/4694837

[8] B.C. Gu, S.W. Baek, H.W. Jegal, S.M. Choi, and W.C. Kim, "Infrared signature characteristic of a microturbine engine exhaust plume," *Infrared Physics & Technology*, Vol. 86, pp. 11-22, 2017. https://doi.org/10.1016/j.infrared.2017.08.014

[9] S.M. Choi, S. Kim, R.S. Myong, and W.C. Kim, "Experimental investigation of infrared signal characteristics in a micro-turboject engine," *The Aeronautical Journal*, Vol. 123, No. 1261, pp. 340-355, 2019. https://doi.org/10.1017/aer.2018.164

[10] S.M. Choi, J.S. Lee, R.S. Myong, H.N. Jo, and J.W. Kim, "Schlieren visualization of micro gas turbine exhaust plume with different shapes of nozzle," *Journal of Visualization*, Vol. 23, No. 4, 2020.

https://doi.org/10.1007/s12650-020-00648-9
[11] J.Y. Choi, H.S. Jang, H.M. Kim, and S.M. Choi, "Plume IR characteristics of microturbine engine in various bypass ratio," *Infrared Physics & Technology*, Vol. 117, 2021.
https://doi.org/10.1016/j.infrared.2021.103846
[12] Y. Zhou, Q. Wang, T. Li, and H. Hu, "A numerical simulation method for aircraft infrared imaging," *Infrared Physics & Technology*, Vol. 83, pp. 68-77, 2017.
https://doi.org/10.1016/j.infrared.2017.04.011
[13] P. Sun, L. Zhou, Z.X. Wang, and X. Sun, "Effect of serpentine nozzle on bypass ratio of turbofan engine exhaust," *Journal of Joint Propulsion Conference*, AIAA 2018-4744, 2018.
https://doi.org/10.2514/6.2018-4744
[14] Q. Zheng, Z. Xu, Y. Wang, F. Sun, and H. Zhang, "Overall optimization design of high temperature components cooling coefficient for lower infrared turbofan engine," *Infrared Physics & Technology,* Vol. 102, 101990, 2019.
https://doi.org/10.1016/j.infrared.2019.102990
[15] J.H. Chae, J.H. Lee, J.W. Lee, N.K. Ha, D.G. Kim, H.S. Jang, and R. S. Myong, "Computational analysis of effects of thermal flow field and chemical components on the IR signature in the exhaust plume of a micro jet engine," *Journal of Computational Fluids Engineering*, Vol. 24, No. 3, pp. 101-111, 2019.
http://dx.doi.org/10.6112/kscfe.2019.24.3.101
[16] S.M. Jo, J.W. Kim, and O.J. Kwon, "A narrow-band k-distribution model with single mixture gas assumption for radiative flows", *Infrared Physics & Technology*, Vol. 91, pp. 27-36, 2018.
https://doi.org/10.1016/j.infrared.2018.03.025
[17] P.J. Marteney, "Experimental investigation of the opacity of small particles," *NASA CR-211*, 1965.
[18] N.L. Krascella, "Theoretical investigation of the absorption and scattering characteristics of small particles," *NASA CR-210*, 1965.
[19] R.D. Harris, K. Dell, G.G. Pippin, S.J. Young, and L.R. Martin, "Study of radiative scattering concept of plume infrared radiation obscuration," *AFOSR-TR-79-0039*, 1979.
https://doi.org/10.21236/ada065006
[20] S.A. Weisrose and G. Shadmon, "Radiative transfer calculations through an aerosol cloud," *Journal of Quantitative Spectroscopy and Radiative Transfer*, Vol. 31, No. 1, pp. 63-70, 1984.
https://doi.org/10.1016/0022-4073(84)90050-5
[21] S.A. Weisrose, R. Davidson, M. Lindner, S. Jacobson, and J. Wallace, "Aerosol effects on jet-engine IR radiation," *International Society for Optics and Photonics*, Vol. 972, pp. 144-160, 1988.
https://doi.org/10.1117/12.948297
[22] G. Parent, P. Boulet, S. Gauthier, J. Blaise, and A. Collin, "Experimental investigation of radiation transmission through a water spray," *Journal of Quantitative Spectroscopy and Radiative Transver*, Vol. 97, No. 1, pp. 126-141, 2006.
https://doi.org/10.1016/j.jqsrt.2004.12.030
[23] Z. Chen, C. Li, L. Zhang, L. Zhang, and H. Chen, "Water spray parameters study with the minimun infrared transmission in the atmospheric windows," *Symposium on Photoelectronic Detection and Imaging 2011: Advances in Infrared Imaging and Applications*, *International Society for Optics and Photonics*, Vol. 8193, 2011.
https://doi.org/10.1117/12.899572
[24] O.K. Voitsekhovskaya, O.V. Shefer, and D.E. Kashirskii, "Criterion of the need to consider the cooperative effect of the molecular absorption and aerosol scattering on calculations of IR transmission function," *International Society for Optics and Photonics*, Vol. 9292, pp. 1-8, 2014.
https://doi.org/10.1117/12.2074458
[25] T.L. Myers, C.S. Brauer, Y. Su, T.A. Blake, T.J. Johnson, and R.L. Richardson, "The influence of particle size on infrared reflectance spectra," *International Society for Optics*

and Photonics, Vol. 9088, pp. 1-8, 2014.
https://doi.org/10.1117/12.2053350
[26] J. Li, Y. Jiang, S. Yu, and F. Zhou, "Cooling effect of water injection on a high-temperature supersonic jet," *Energies*, Vol. 8, No. 11, pp. 13194-13210, 2015.
https://doi.org/10.3390/en81112363
[27] X. Liu, Y. Liu, Q. Peng, F. Jie, and D. Ming, "Calculation of attenuation of infrared radiation energy by ship water mist," *2019 IEEE 8th Joint International Information Technology and Artificial Intelligence Conference*, pp. 807-811, 2019.
https://doi.org/10.1109/ITAIC.2019.8785527
[28] J.W. Lee, Y.R. Lee, J.W. Kim, and R.S. Myong, "Analysis of characteristics of aircraft nozzle flow by injecting water mist," *Journal of Computational Fluids Engineering*, Vol. 25, No. 3, pp. 102-112, 2020.
https://doi.org/10.6112/kscfe.2020.25.3.102
[29] Y. Zuo, L. Guo, and D. Xiao, "The near-field scattering of chaff cloud," *2018 Cross Strait Quad-Regional Radio Science and Wireless Technology Conference IEEE*, pp. 1-4, 2018.
https://doi.org/10.1109/CSQRWC.2018.8455545
[30] E.H. Newman and K. Kingsley, "An introduction to the method of moments," *Computer Physics Communications*, Vol. 68, No. 1, pp. 1-18, 1991.
https://doi.org/10.1016/0010-4655(91)90191-M
[31] S.M. Rao, D. R. Wilton, and A.W. Glisson, "Electromagnetic scattering by surfaces of arbitrary shape," *IEEE Transactions on Antennas and Propagation*, Vol. 30, pp. 409-418, 1982.
https://doi.org/10.1109/TAP.1982.1142818
[32] Altair FEKO User Guide v.2020.1.
[33] W.C. Gibson, *The Method of Moments in Electromagnetics*, Chapman & Hall/CRC, 2008.
[34] ANSYS FLUENT User's Manual v19.1.
[35] J. Yi, Y. Ma, W. Wang, and L. Shao, "Inhibition effect of water injection on afterburning of rocket motor exhaust plume," *Chinese Journal of Aeronautics*, Vol. 23, No. 6, pp. 653-659, 2010.
https://doi.org/10.1016/S1000-9361(09)60267-3
[36] A.J.M. Heselden and P.L. Hinkley, "Measurements of the transmission of radiation through water spray," *Fire Technology*, Vol. 1, No. 2, pp. 130-137, 1965.
[37] L.F. Chen, C.K. Neo, C.P. Varadan, and V.K. Varadan, *Microwave Electronics: Measurement and Materials Characterization*, John Wiley & Sons, 2004.
[38] M.E. Whitson Jr, "Handbook of the infrared optical properties of Al_2O_3, carbon, MGO, and ZrO_2. Volume 1," *SAMSO-TR-75-131*, Space and Missile Systems Organization, LA, US, 1975.
[39] F. Wooten, *Optical Properties of Solids*, Academic Press, 2013.
[40] G.H. Dai, Z.B. Ren, Q. Sun, and J. Liu, "Study of Mie extinction efficiency," In ICO20: Optical Information Processing International Society for Optics and Photonics, Vol. 6027, pp. 602723-602728, 2006.
https://doi.org/10.1117/12.668195